ISET Journal of Earthquake Technology, Paper No. 427, Vol. 39, No. 4, December 2002, pp. 273-310

EMPIRICAL SCALING OF STRONG EARTHQUAKE GROUND MOTION - PART III: SYNTHETIC STRONG MOTION

V.W. Lee
Civil Engineering Department
University of Southern California
Los Angeles, California, U.S.A.

ABSTRACT

A comprehensive and general method for the prediction of strong motion amplitudes, developed by Strong Motion Research Group at University of Southern California, is reviewed. It uses synthetic translational accelerograms and the theory of linear wave propagation to predict all other components of strong motion: rotations (torsion and rocking), strains and curvatures. It gives site-specific synthetic motions which have realistic non-stationary frequency content, site-specific dispersion properties, and amplitudes and the duration which are compatible with empirical scaling equations developed for the estimation of strong motion in California.

KEYWORDS: Dispersion, Rayleigh and Love Modes, Translation, Torsion, Rocking

INTRODUCTION

For many applications, it is necessary to estimate future shaking at a particular site which is outside the range of strong-motion parameters for which the existing recorded data is available. This happens, in particular, in those parts of the world where recorded data is not yet available. Considerable variability in the characteristics of recorded strong-motions recorded under similar conditions, may require a characterization of future shaking in terms of an ensemble of accelerograms rather than in terms of just one or two "typical" records. In many earthquake engineering analyses, particularly those which deal with the non-linear response of structures, the entire analysis must be performed in the time domain, because the superposition techniques do not apply. This and many related situations have thus created a need for the development of techniques for the generation of synthetic (artificial) strong-motion time histories that simulate realistic ground motions. In this work, we will review the only complete and comprehensive family of papers which outline the methods for generation of artificial time histories of (1) translational acceleration, (2) rotational acceleration (torsion and rocking), (3) surface strain, and (4) surface curvature.

Apparent irregularity of early recorded accelerograms and the limited number of records in the 1950's have led investigators to explore the possibility of modeling strong ground shaking by means of random time functions of simple but known properties. Housner (1955), for example, assumed that an accelerogram could be modeled by a series of one-cycle sine-wave pulses; others used a series of pulses distributed randomly in time (Goodman et al., 1955; Rosenblueth, 1956; Bycroft, 1960; Rosenblueth and Bustamante, 1962). On the basis of such artificial time functions of known statistical properties, it became clear (Bolotin, 1960) that the nonstationarity of ground motion can influence structural response significantly. This prompted the development of methods for the construction of artificial accelerograms by using nonstationary random time series (e.g., Bogdanoff et al., 1961; Amin and Ang, 1966; Goto and Toki, 1969). The nonstationarity in these models was achieved typically by (a) multiplying stationary random time series by a nonstationary envelope function, (b) changing the frequency content of an artificial accelerogram as a function of time, and by (c) superimposing simple earthquake sources with some phase delays in time (e.g., Rascon and Cornell, 1969) to represent the propagation of a simple earthquake source (e.g., Honda, 1957) by means of radiated P and S waves only.

Observational studies of strong ground motion in the 1970's showed that a typical strong motion record consists of near-field, intermediate-field, body and surface waves contributing different amounts to the total result, depending on the earthquake source mechanism and on the wave path (Trifunac, 1971a, 1971b; Trifunac, 1972a, 1972b; Trifunac, 1973). Empirical studies of spectral characteristics (Trifunac, 1976, 1979a, 1979b, 1993, 1994, 1995a, 1995b; Trifunac and Anderson, 1977; Trifunac and Lee, 1978, 1985) and frequency-dependent duration (Trifunac and Westermo, 1976a, 1976b; Trifunac and Novikova,

1994, 1995) have further shown the nature of the dependence of strong motion on the geologic environment of the recording station. Consequently, realistic artificial accelerograms must have nonstationary frequency, amplitude and duration characteristics that agree with the trends present in the recorded accelerograms.

In choosing a suitable accelerogram for a particular analysis, many factors must be taken into account, for example, the distance between the source and the site, the size of the earthquake, and the geology surrounding the site. The recorded accelerograms cannot be modified in a simple way to satisfy the requirements at all sites (Lee and Trifunac, 1989), and thus, site-dependent artificial accelerograms are needed.

The majority of the proposed methods for the generation of synthetic accelerograms fall into two categories: (1) methods that utilize random functions, and (2) methods that involve source mechanism and wave propagation models. Using the former methods, the resulting accelerograms do not always have a correct frequency content for engineering applications, and the frequency characteristics of the time record are often uniform from beginning to the end of the record. For a recorded accelerogram, the frequency contained in the beginning of the record (during the arrival of body and high-frequency surface waves) is generally higher. Using the latter methods, a more physically consistent record can be generated, but it is impossible to model all the details of the source as well as of the wave path adequately for the complete frequency range of interest (e.g., 0.5-30 Hz). Because of the simplifications, the generated records often lack proper high-frequency characteristics, when compared with the recorded accelerograms.

This work reviews a unique and comprehensive group of methods for constructing synthetic accelerograms, which have a given Fourier amplitude spectrum, $F(\omega)$, and a given duration. The Fourier amplitude spectrum and the duration can be obtained from correlations with the earthquake parameters. The times of arrival of the waves can be derived from the dispersive properties of the site. This introduces the specific characteristics of each site into the resulting artificial records of strong motion.

GENERATION OF SYNTHETIC TRANSLATIONAL ACCELEROGRAMS

The synthetic translational components of acceleration are constructed to have a required Fourier amplitude spectrum, $FS(\omega)$, and a given duration, $D(\omega)$, at the site. For completeness in this presentation, a review of the method first proposed by Trifunac (1971b), and later refined by Wong and Trifunac (1978, 1979), for the generation of synthetic accelerograms is briefly summarized as follows.

1. Dispersion Curves at a Site

For a given site, a profile with equivalent layered medium is first determined. A model can have L layers. For each layer i, with $i = 1$ to L, the parameters h_i, α_i, β_i and ρ_i must be specified, where $h_i =$ thickness of the $i-$th layer, $\alpha_i = P-$wave velocity, $\beta_i = S-$wave velocity, and $\rho_i =$ density of the medium, with the bottom $(i = L)$ medium of infinite thickness.

In such a medium, surface waves will travel in a dispersive manner, and this will, in general, depend on (1) the material properties of the medium, (2) the frequency of the wave motion, and on (3) the thicknesses of different layers.

Through calculations for the group and phase velocities of the Rayleigh and Love surface waves, the dispersion curves can be evaluated. The results will be given for each mode of Rayleigh and Love surface waves separately, and will consist of phase and group velocities, $C_m(\omega_n)$ and $U_m(\omega_n)$, for a given set of selected frequencies, ω_n, $n = 1, 2, ..., N$.

2. Arrival Times

Once the dispersion curves have been computed, the arrival time of the $m-$th mode at frequency ω_n can be written as

$$t^*_{nm}(R) = R/U_m(\omega_n) \tag{1}$$

where, R is the epicentral distance from the source to the site. For computational efficiency, Equation (1) will be assumed to hold not only at frequency ω_n, but at a frequency band $\omega_n \pm \Delta\omega_n$, which is narrow enough for $U_m(\omega)$ to be assumed constant.

3. Contribution of the Modes at a Given Frequency Band

Within the frequency band $\omega_n \pm \Delta\omega_n$, the $m-$th mode of surface waves is assumed to have a Fourier transform

$$A_{nm}(\omega) = \begin{cases} \dfrac{\pi}{2} A_{nm} e^{-i\left[(\omega-\omega_n)t^*_{nm}+\phi_n\right]} & |\omega-\omega_n| \le \Delta\omega_n \\ 0 & \text{otherwise} \end{cases}$$
$$A_{nm}(-\omega) = A^*_{nm}(\omega) \tag{2}$$

where, ϕ_n is the phase. It is introduced to model the source randomness and other effects along the path. t^*_{nm} is the arrival time of the $m-$th mode given in Equation (1). A_{nm} is the relative amplitude of the $m-$th mode. The phase ϕ_n will be assumed to be a random number between $-\pi$ and π. The relative amplitude A_{nm} will be described in the next section.

The inverse transform of (2) is given by

$$a_{nm}(t) = \frac{1}{2\pi}\int_{-\infty}^{\infty} A_{nm}(\omega) e^{i\omega t} d\omega, \tag{3a}$$

which can be calculated to be

$$a_{nm}(t) = A_{nm}\frac{\sin\Delta\omega_n(t-t^*_{nm})}{(t-t^*_{nm})}\cos(\omega_n t+\phi_n) \tag{3b}$$

This represents the contribution of the $m-$th mode at the given frequency band. The total contribution of all the modes is then given by

$$a_n(t) = \sum_{m=1}^{M}\alpha_n a_{nm}(t) = \sum_{m=1}^{M}\alpha_n A_{nm}\frac{\sin\Delta\omega_n(t-t^*_{nm})}{(t-t^*_{nm})}\cos(\omega_n t+\phi_n), \tag{3c}$$

where, M is the total number of wave modes, and α_n is the scaling factor used to determine the final amplitude of $FS(\omega_n)$, as described in the next sub-section.

4. Determination of A_{nm} and α_n

Relative amplitudes of different modes of surface waves, A_{nm}, depend on the source mechanism and the propagation path, and are difficult to be estimated in a general case. Hence, it is useful to estimate these amplitudes empirically on the basis of previous acceleration recordings.

The following empirical equations for A_{nm} have been suggested by Trifunac (1971b)

$$A_{nm}(\omega_n) = A_1(m)A_2(\omega_n) \tag{4}$$

where,

$$A_1(m) = \left|\exp\left(-(m-m_0)^2/2C_0^2\right) + C_R X_m\right| \tag{5}$$

and

$$A_2(\omega_n) = \left|B_0\exp\left(-(\omega_n-\omega_p)^2/2\omega_B^2\right) + B_R X_n\right| \tag{6}$$

with X_m and X_n being random numbers between -1 and 1, and the values of other constants are suggested in Table 1.

Table 1: Empirical Scaling Coefficients for Equations (5) and (6) (from Trifunac, 1971a, 1971b)

Mode	C_0	m_o	C_R	B_0	ω_p	ω_B	B_R
1	3	5	0.2	1.5	10	5	0.1
2	3	5	0.2	1.5	10	5	0.1
3	3	5	0.2	1.5	10	5	0.1
4	3	5	0.2	2.0	25	15	0.1
5	3	5	0.2	2.0	25	15	0.1
6	3	6	0.2	3.0	30	10	0.3
7	3	7	0.2	1.5	30	5	0.25

The scaling factor α_n is next determined, by using the empirically determined Fourier amplitudes. The Fourier amplitude of $a_n(t)$ in Equation (3c) is given by

$$\left|A_n(\omega)\right| = \begin{cases} \left|\sum_{m=1}^{M} \frac{\pi}{2} \alpha_n A_{nm} \exp\left[-i\left(\left(\omega-\omega_n\right)t_{nm}^{*}-\phi_n\right)\right]\right|, & \left|\omega-\omega_m\right| < \Delta\omega_n \\ 0 & \text{otherwise} \end{cases} \tag{7}$$

for $0 \le \omega < \infty$, and $\left|A_n(-\omega)\right| = \left|A_n(\omega)\right|$.

It is seen that the amplitude $\left|A_n(\omega)\right|$ is defined only over the narrow band of width $2\Delta\omega_n$. Its mean amplitude over this band is given by

$$\overline{\left|A_n(\omega)\right|} = \frac{1}{2\Delta\omega_n} \int_{\omega_n-\Delta\omega_n}^{\omega_n+\Delta\omega_n} \left|A_n(\omega)\right| d\omega \tag{8}$$

which should agree with the empirically estimated Fourier amplitude, $\hat{FS}(\omega_n)$,

$$\overline{\left|A_n(\omega)\right|} = \hat{FS}(\omega_n) \tag{9}$$

Combining Equations (7), (8) and (9), α_n becomes

$$\alpha_n = \frac{2\Delta\omega_n \hat{FS}(\omega_n)}{\frac{\pi}{2}\int_{\omega_n-\Delta\omega_n}^{\omega_n+\Delta\omega_n} \left|\sum_{m=1}^{M} A_{nm} \exp\left[-i\left(\left(\omega-\omega_n\right)t_{nm}^{*}-\phi_n\right)\right]\right| d\omega} \tag{10}$$

The Fourier amplitude $\hat{FS}(\omega_n)$ at frequency ω_n may be estimated from empirical scaling equations, by using the earthquake parameters specified at the site. These parameters may include a suitable combination of the following: M = local magnitude M_L or surface wave magnitude M_S (Richter, 1958), R = epicentral distance, MMI = modified Mercalli intensity at the site, s = geological site classification (s = 0, 1 or 2), S_L = geotechnical site classification, h = depth of sediments, and v = component direction ($v = 0$: horizontal; $v = 1$: vertical).

5. The Total Accelerogram

The total accelerogram can be expressed as

$$a(t) = \sum_{n=1}^{N} a_n(t) \tag{11}$$

where, N is the total number of frequency bands. From Equation (3), (11) becomes

$$a(t) = \sum_{n=1}^{N} \left(\sum_{m=1}^{M} A_{nm} \frac{\sin \Delta\omega_n \left(t - t_{nm}^*\right)}{t - t_{nm}^*} \right) \alpha_n \cos\left(\omega_n t + \phi_n\right) \tag{12}$$

One final property, the duration or 'length' of $a(t)$, will be determined by using the empirical results on strong motion duration (Trifunac and Brady, 1975; Trifunac and Novikova, 1994) and the first and last arrival times of the waves.

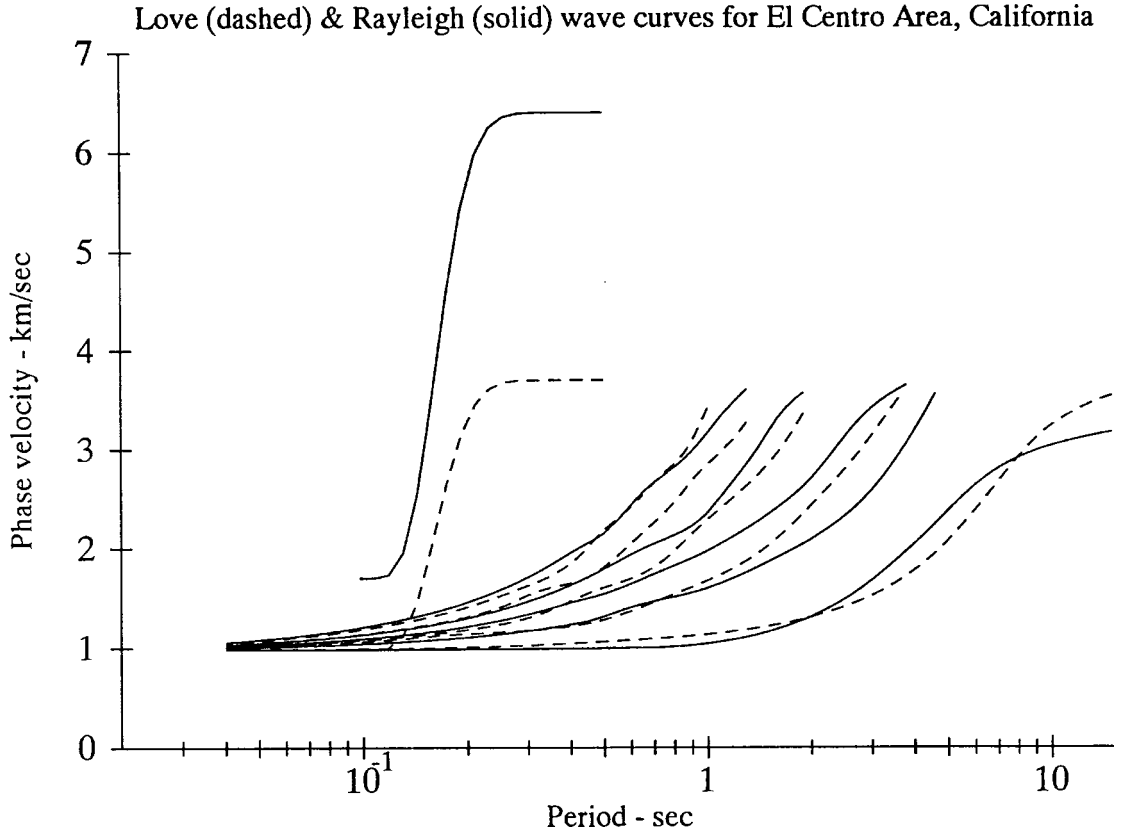

Fig. 1 Love and Rayleigh waves curves for El Centro Area, California: phase velocity

6. Example of Synthetic Accelerograms

To illustrate synthetic accelerograms, we choose the site at Westmoreland in Imperial Valley, California. Dispersion curves for this site were computed assuming the properties of layered medium in Table 2.

Table 2: Properties of the Layered Medium Adopted to Represent the Site Properties in the Area of Westmoreland in Imperial Valley, California

Layer #	Depth (km)	P-Wave Velocity (km/sec)	S-Wave Velocity (km/sec)	Density (gm/cm^3)
1	0.18	1.70	1.98	1.28
2	0.55	1.96	1.13	1.36
3	0.98	2.71	1.57	1.59
4	1.19	3.76	2.17	1.91
5	2.68	4.69	2.71	2.19
6	∞	6.40	3.70	2.71

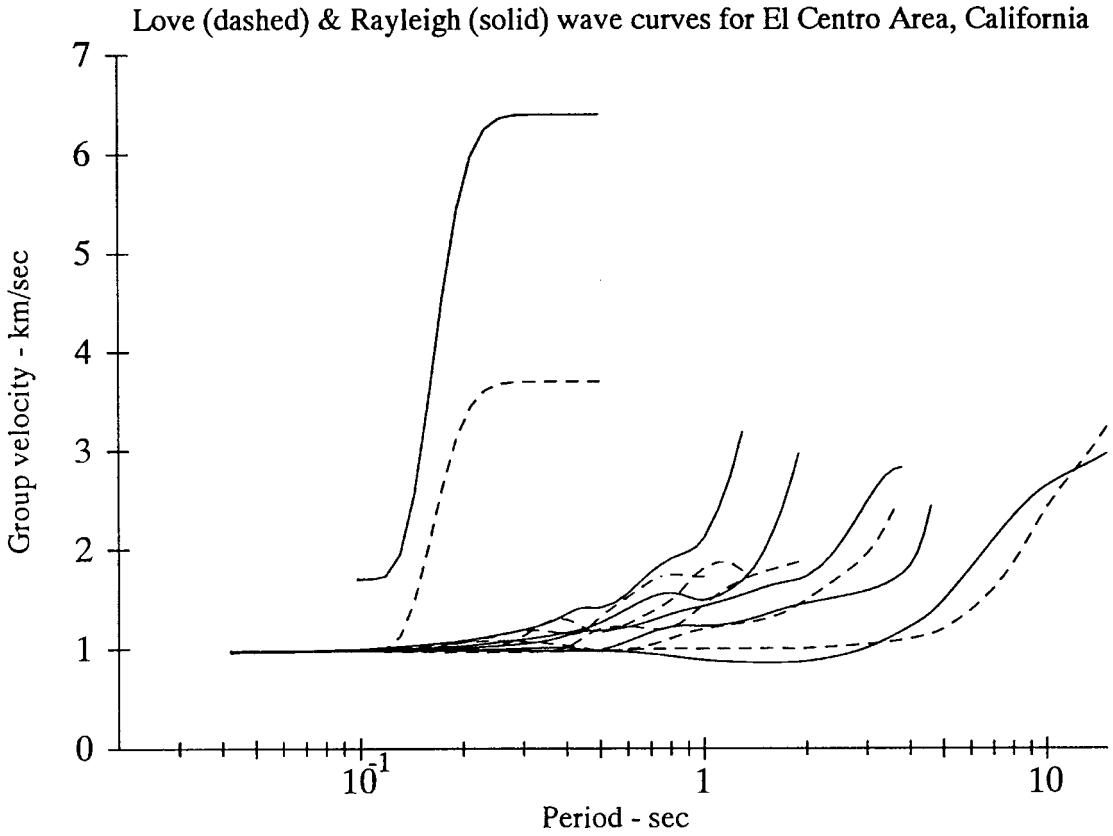

Fig. 2 Love and Rayleigh waves curves for El Centro Area, California: group velocity

Figure 1 shows the Rayleigh- and Love-wave phase velocities (in km/sec) versus the period of the waves (in seconds). The 5 solid curves are for the first 5 modes of the Rayleigh waves. Mode 1 is the rightmost solid curve, and mode 5 is next to the leftmost solid curve, with the intermediate modes in between. The same holds for the modes of Love waves. At low periods, all the curves approach the minimum $S-$wave velocity (0.98 km/s at this site). Figure 2 shows the corresponding group velocity curves. The two curves at the extreme left in Figures 1 and 2 approximately model the arrival of the wave components associated with the incident P and S waves.

The following earthquake parameters are chosen for this site, as input for the computer program SYNACC (Wong and Trifunac, 1978): earthquake magnitude, $M = 6.5$, epicentral distance, D = 10.0 km, confidence level, $p = 0.5$, site condition, s = 0 (alluvium), and component direction, v = 0 (horizontal).

Figure 3 shows a plot of the synthetic translational acceleration, and the velocity and displacement time-histories calculated from it. Figure 4 presents the corresponding response and Fourier spectra.

THE TORSIONAL COMPONENT OF EARTHQUAKE GROUND MOTIONS

The importance of torsional and rocking excitations has been indicated by the studies of Dravinski and Trifunac (1979, 1980), Kobori and Shinozaki (1975), Luco (1976), Bielak (1978), Lee (1979), Gupta and Trifunac (1987, 1988, 1990a, 1990b, 1990c, 1991), Todorovska and Lee (1989), and Todorovska and Trifunac (1989, 1990a, 1990b, 1992, 1993). With the slow development of strong-motion instruments that record rotational components of strong motions (Hudson, 1983; Trifunac and Todorovska, 2001), it becomes necessary to explore the possibility of estimating those in terms of the corresponding translational components of strong shaking.

By considering the horizontal propagation of plane waves with constant velocity C, Newmark (1969) estimated the contribution to the displacements of building foundation, resulting from torsional earthquake ground motions. Tso and Hsu (1978) used a similar approach, in addition to assuming that the motions also included plane non-dispersive waves. Nathan and MacKenzie (1975) discussed the possible

averaging effects of foundation sizes on the resulting torsional excitations of buildings. These investigations, however, failed to consider the dependence of the phase velocity on the frequencies of the incoming Love waves. Their assumption that the incoming waves are of constant phase velocity at all frequencies, makes their results useless. Lee and Trifunac (1985) included the effects of wave dispersion and transient arrivals in the estimation of torsional accelerograms in an elastic layered half-space. The earlier work of Trifunac (1982) in calculating the torsional component of incident plane SH-waves was extended to enable the calculation of torsion from surface Love waves.

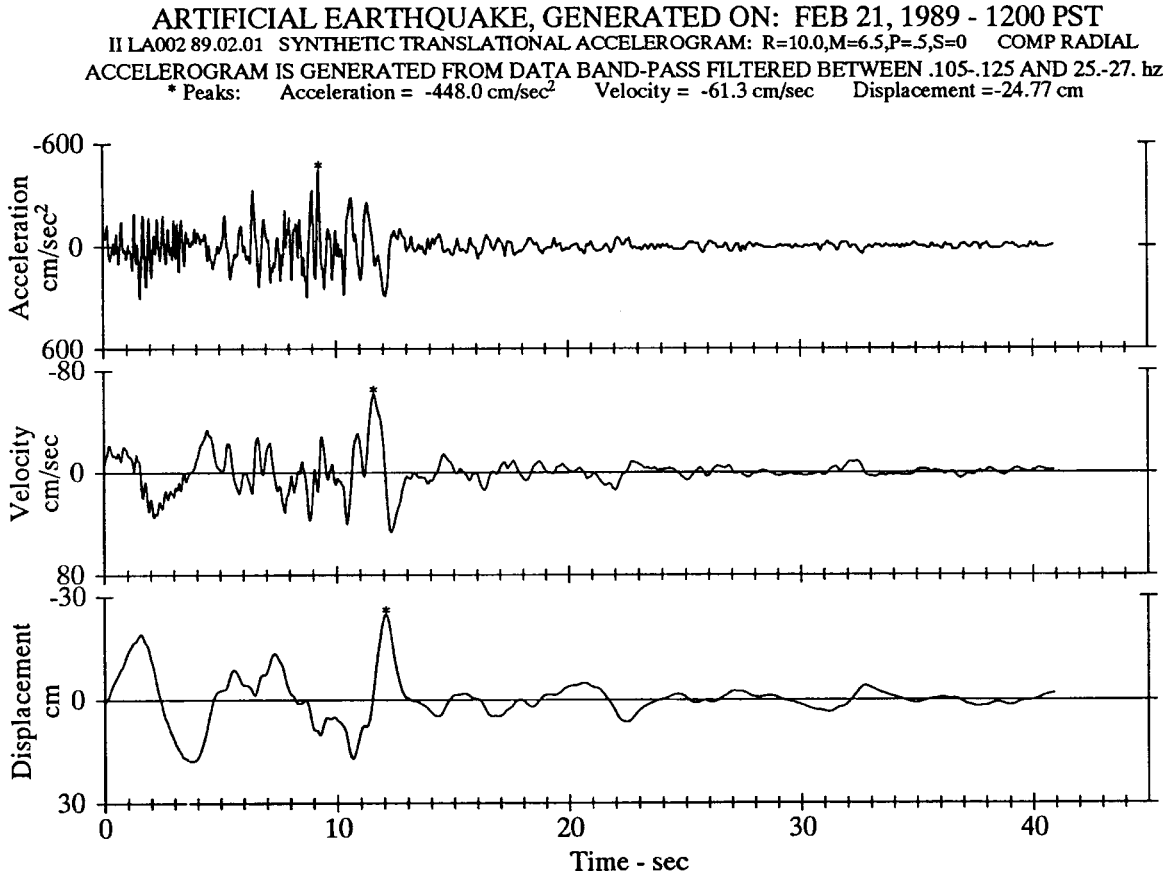

Fig. 3 Artificial earthquake synthetic translational accelerogram

1. The Torsional Motion of Incident Waves

Figure 5 shows the rectangular coordinate system (x_1, x_2, x_3) with the incident and reflected plane SH-waves, in the presence of the stress-free boundary $(x_2 = 0)$, at the surface of the elastic, homogeneous and isotropic half space $(x_2 \le 0)$. The particle motions of the waves are in the x_3 – direction.

The incident SH-wave is assumed to have amplitude A_0 and angle of incidence θ_0 (Figure 5). The reflected wave will also have amplitude A_0 and the same angle of reflection θ_0. The resulting motion is

$$\begin{aligned} u_3 &= \left[A_0 e^{ik(x_1 \sin\theta_0 + x_2 \cos\theta_0)} + A_0 e^{ik(x_1 \sin\theta_0 - x_2 \cos\theta_0)}\right] e^{-i\omega t} \\ &= 2A_0 \cos(kx_2 \cos\theta_0) e^{ikx_1 \sin\theta_0} e^{-i\omega t} \end{aligned} \tag{13}$$

with ω being the frequency of the incoming wave, with velocity β, and $k = \omega/\beta$, the corresponding wave number. The torsional component of motion associated with the SH-waves at the half-space surface $(x_2 = 0)$ is (Trifunac, 1982):

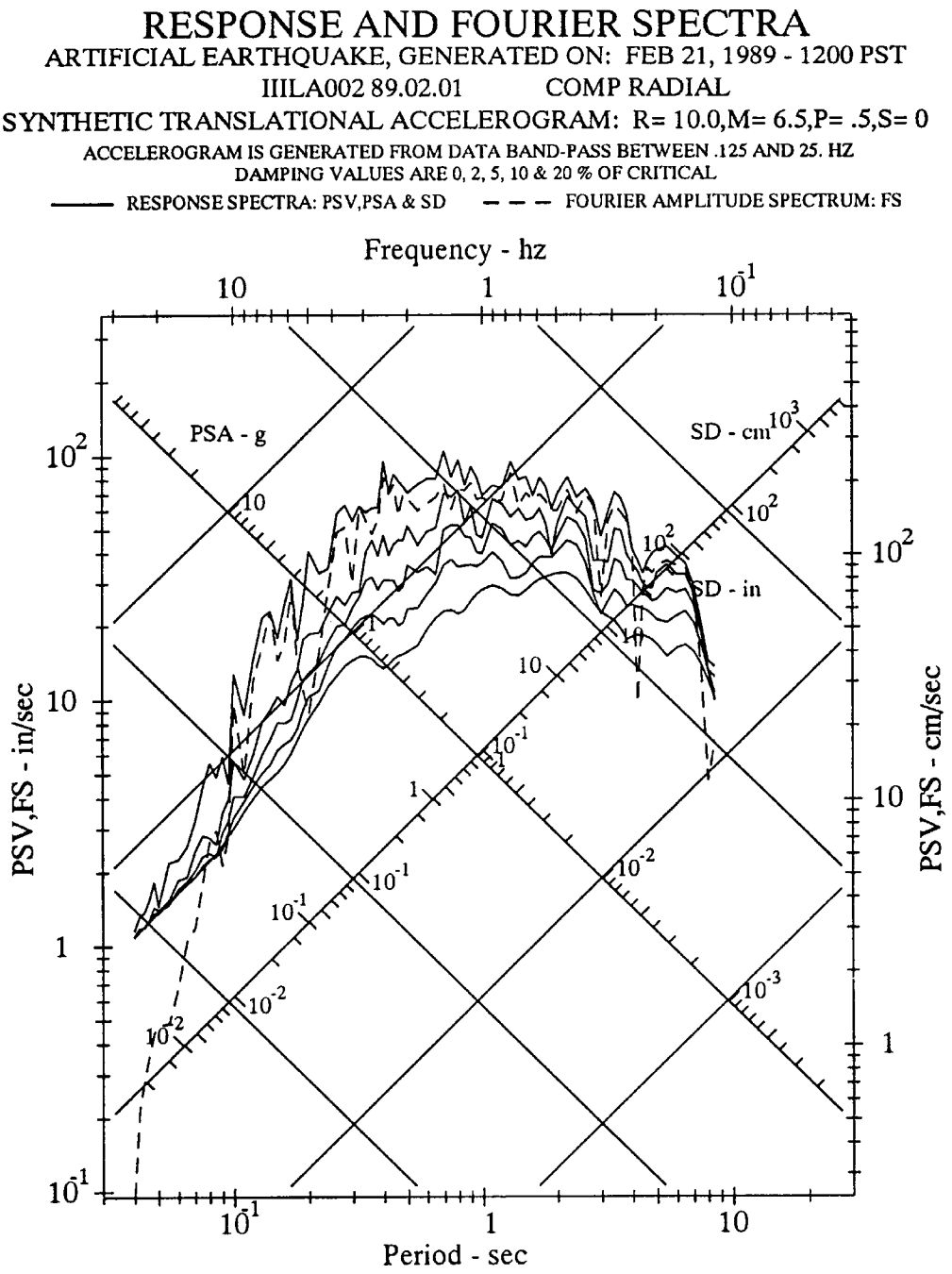

Fig. 4 Artificial earthquake synthetic translational response and Fourier spectra

$$
\begin{aligned}
\psi_{13}\big|_{x_2=0} &= \left(\frac{1}{2}\tilde{\Delta}\times\tilde{u}\right)\times\hat{e}_2 = -\frac{1}{2}\frac{\partial u_3}{\partial x_1} \\
&= -A_0 ik\sin\theta_0 e^{ikx_1\sin\theta_0} \\
&= -\frac{1}{2}ik\sin\theta_0 u_3 \\
&= \frac{k\sin\theta_0}{2}u_3 e^{-i\pi/2}
\end{aligned}
\tag{14}
$$

It is seen that the torsional motion has a phase shift of $-\pi/2$ relative to the translational motion. From Equation (14), one can define the amplitude ratio,

$$\left|\frac{\psi_{13}}{u_3}\right| = \frac{k\sin\theta_0}{2} = \frac{1}{2}\frac{\omega}{\beta}\sin\theta_0 = \frac{1}{2}\frac{\omega}{c_x} \tag{15}$$

where, $c_x = \beta/\sin\theta_0$ is the phase velocity in the horizontal (x_1) direction. Including the phase shift, Equation (14) can be rewritten as

$$\psi_{13}\Big|_{x_2=0} = \frac{1}{2}\frac{\omega}{c_x}u_3 e^{-i\pi/2} \tag{16}$$

which shows that at the ground surface $(x_2 = 0)$, the amplitude of torsional motion increases linearly with frequency, ω.

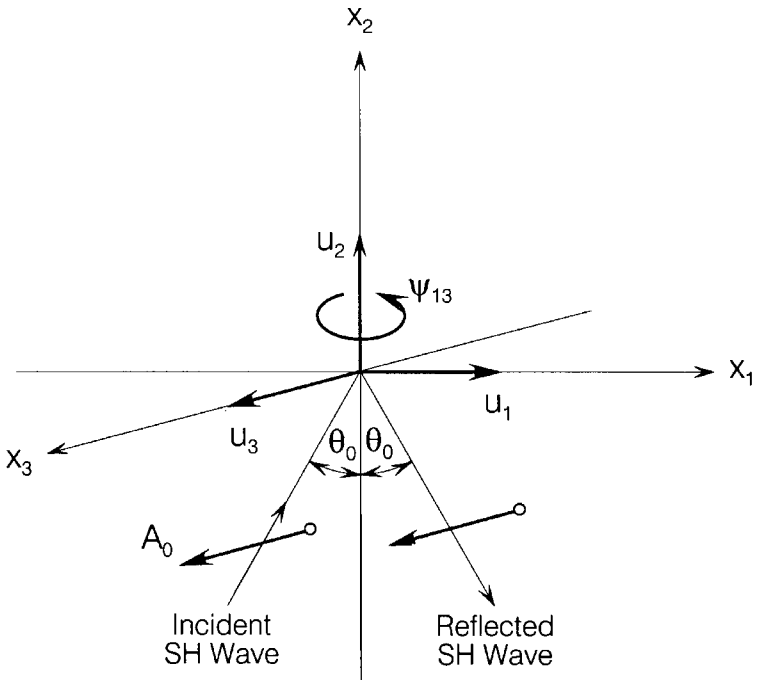

Fig. 5 Incident SH wave on half-space

2. Estimation of Synthetic Torsional Motion

Recording of the rotational components of strong motion is at present limited only to a few experimental programs (Shibata et al., 1976; Trifunac and Todorovska, 2001). It is not very likely that a significant amount of such data will, in the near future, be available for empirical and theoretical analyses. It thus becomes necessary to explore the possibility of estimating torsional acceleration in terms of the corresponding translational components of strong motion, along with the information on the types and the direction of approach of the incident waves.

Expressing the strong earthquake translational ground motion in terms of the Fourier amplitude spectrum, the Fourier amplitude spectrum of the corresponding torsional motion can be estimated by using Equation (16). By employing this result in conjunction with the method for the synthesis of artificial translational accelerograms, as described in the previous section, the complete time-history of synthetic torsional motion can be constructed.

From Equation (2), the $m-$ th mode of surface waves, within the frequency band $\omega_n \pm \Delta\omega_n$, has the Fourier transform of the translational motion given by

$$A_{nm}(\omega) = \begin{cases} \dfrac{\pi}{2} A_{nm} e^{-i\left[(\omega-\omega_n)t^*_{nm}+\phi_0\right]} & |\omega-\omega_n| \le \Delta\omega_n \\ 0 & \text{otherwise} \end{cases}$$

and (17)

$$A_{nm}(-\omega) = A^*_{nm}(\omega)$$

The corresponding Fourier transform of the rotational motion is thus given by

$$\Psi_{nm}(\omega)=\begin{cases}\dfrac{\omega\pi}{4C_{nm}}A_{nm}e^{-i\left[(\omega-\omega_n)t^*_{nm}+\phi_n+\pi/2\right]} & |\omega-\omega_n|\le\Delta\omega_n\\ 0 & \text{otherwise}\end{cases} \tag{18}$$

where, $C_{nm}=C_m(\omega_n)$ is the phase velocity of the $m-$th mode of surface Love waves, assumed to be constant within the frequency band $\omega_n\pm\Delta\omega_n$. The total contribution from all the modes of Love waves to the rotational motion in this frequency band is

$$\Psi_{n}(\omega)=\begin{cases}\dfrac{\alpha_n\omega\pi}{4}\sum_{m=1}^{M}\dfrac{A_{nm}}{C_{nm}}e^{-i\left[(\omega-\omega_n)t^*_{nm}+\phi_n+\pi/2\right]} & |\omega-\omega_n|\le\Delta\omega_n\\ 0 & \text{otherwise}\end{cases} \tag{19}$$

where, α_n is the scaling factor, as given in Equation (10).

The total Fourier transform of the rotational accelerogram is then given by

$$\Psi(\omega)=\sum_{n=1}^{N}\Psi_n(\omega) \tag{20}$$

where, N is the total number of frequency bands considered. The ratio of the Fourier amplitude of the rotational acceleration to that of the translational motion thus takes the form

$$\left|\frac{\Psi(\omega)}{A(\omega)}\right|=\left|\frac{\Psi_n(\omega)}{A_n(\omega)}\right| \tag{21}$$

for the frequencies within the frequency band $\omega_n\pm\Delta\omega_n$. On simplifying, Equation (21) takes the form

$$\left|\frac{\Psi(\omega)}{A(\omega)}\right|=\frac{\omega}{2}\left|\frac{\sum_{m=1}^{M}\dfrac{A_{nm}}{C_{nm}}e^{-(\omega-\omega_n)t^*_{nm}}}{\sum_{m=1}^{N}A_{nm}e^{-(\omega-\omega_n)t^*_{nm}}}\right|;\ |\omega-\omega_n|\le\Delta\omega_n \tag{22}$$

and, in particular for $\omega=\omega_n$,

$$\left|\frac{\Psi(\omega)}{A(\omega)}\right|_{\omega=\omega_n}=\frac{\omega_n}{2}\frac{\sum_{m=1}^{M}A_{nm}/C_{nm}}{\sum_{m=1}^{M}A_{nm}} \tag{23}$$

An asymptotic expansion of Equation (23) for large and small frequencies is possible. At the high-frequency end, the phase velocities of all modes of surface waves approach $\beta_{\min}$, the minimum shear wave velocity in the layered model. Thus

$$\left|\frac{\Psi(\omega)}{A(\omega)}\right|\sim\frac{\omega_n}{2}\left|\frac{\sum_{m=1}^{M}A_{nm}/\beta_{\min}}{\sum_{m=1}^{M}A_{nm}}\right|=\frac{\omega_n}{2\beta_{\min}} \tag{24}$$

$$\text{as } \omega_n\to\infty$$

At the low-frequency end, essentially the only mode present in the layered model is the first mode, and its phase velocity approaches $\beta_{\max}$, the maximum shear wave velocity in the layered medium. Thus,

$$\left|\frac{\Psi(\omega)}{A(\omega)}\right|\sim\frac{\omega_n}{2}\left|\frac{A_{n1}/\beta_{\max}}{A_{n1}}\right|=\frac{\omega_n}{2\beta_{\max}} \tag{25}$$

$$\text{as } \omega_n\to 0$$

It is noted that from the dimensional analysis point of view, Equations (24) and (25) agree with the equations proposed by Newmark (1969). However, it is seen that the "velocity" representing the overall

average trend of the ratio $|\Psi(\omega)/A(\omega)|$ is not constant. It changes from $\beta_{\min}$ (for $\omega \to \infty$) to $\beta_{\max}$ (for $\omega \to 0$), the velocity in the half-space beneath the surface layers.

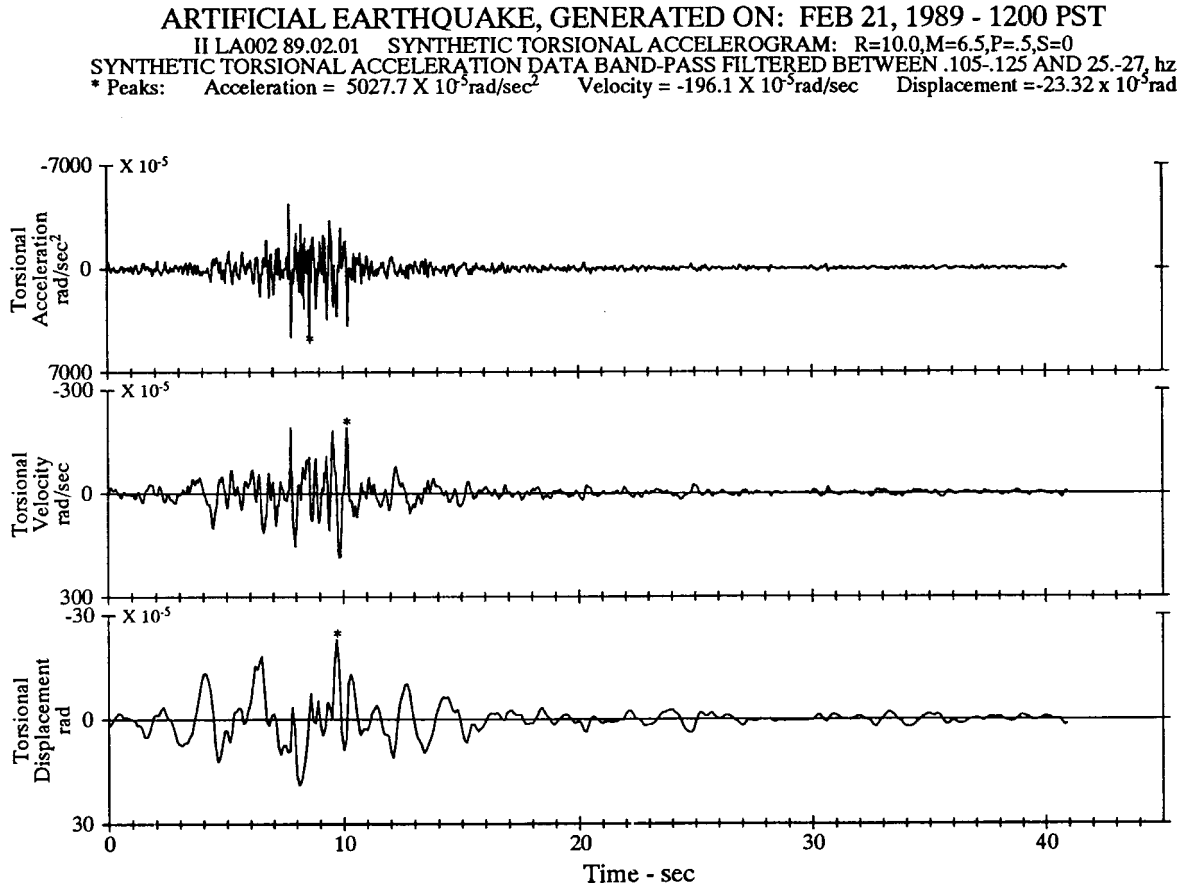

Fig. 6 Artificial earthquake synthetic torsional accelerogram

3. Examples of Synthetic Torsion

Following the analysis in the previous sections, one can generate the translational (horizontal and vertical) and torsional accelerograms simultaneously. For illustration, the same site at Westmoreland in Imperial Valley is used, as in Sub-section 6 of the previous section. Thus, the same dispersion curves for this site are used here.

Figure 6 gives a plot of the synthetic torsional acceleration, velocity and displacement, with units in rad/s^2, rad/s and rad, respectively. Figure 7 presents the corresponding torsional response and Fourier spectra. As in the case of the response spectra for the translational accelerogram, the torsional response spectra represent the maximum torsional response of single-degree-of-freedom systems of specified natural periods and damping ratios, when subjected to the torsional accelerogram as input. The units for torsional displacement, SD, pseudo relative velocity, PSV, and relative pseudo acceleration, PSA, are rad, rad/s, and rad/s^2, respectively.

Figure 8 shows the ratio of torsional to translational response for different periods and damping ratios. As indicated by Equation (16), the ratio is high at the high-frequency (short-period) end, and decreases almost linearly towards the low-frequency (long-period) end. The Fourier spectrum (dashed line) also starts out with the large ratio at the high-frequency end, and progressively decreases to the small ratios at the low-frequency (long-period) end. The five solid curves correspond to the damping values of 0, 2, 5, 10 and 20% of critical. At the high-frequency end, the zero damping curve has a higher ratio than the 2, 5, 10 and 20% curves. The ratios for all five damping ratios decrease progressively with decreasing frequency (increasing period), with the order of the ratios switched at the low-frequency end, so that the 20% damping curve ends up with the highest ratio, followed by 10%, 5%, 2% and 0% curves, with the ratio for the Fourier spectrum being the lowest on average.

Figure 9 shows the ratios of torsional to translational Fourier spectrum amplitudes, as calculated from Equation (23). The dashed line joining the high- and low-frequency asymptotic limits, connects the amplitudes given by Equations (24) and (25). Comparison with Figure 8 shows that this straight line approximates the overall trend of the ratios of torsional to translational spectral amplitudes very well.

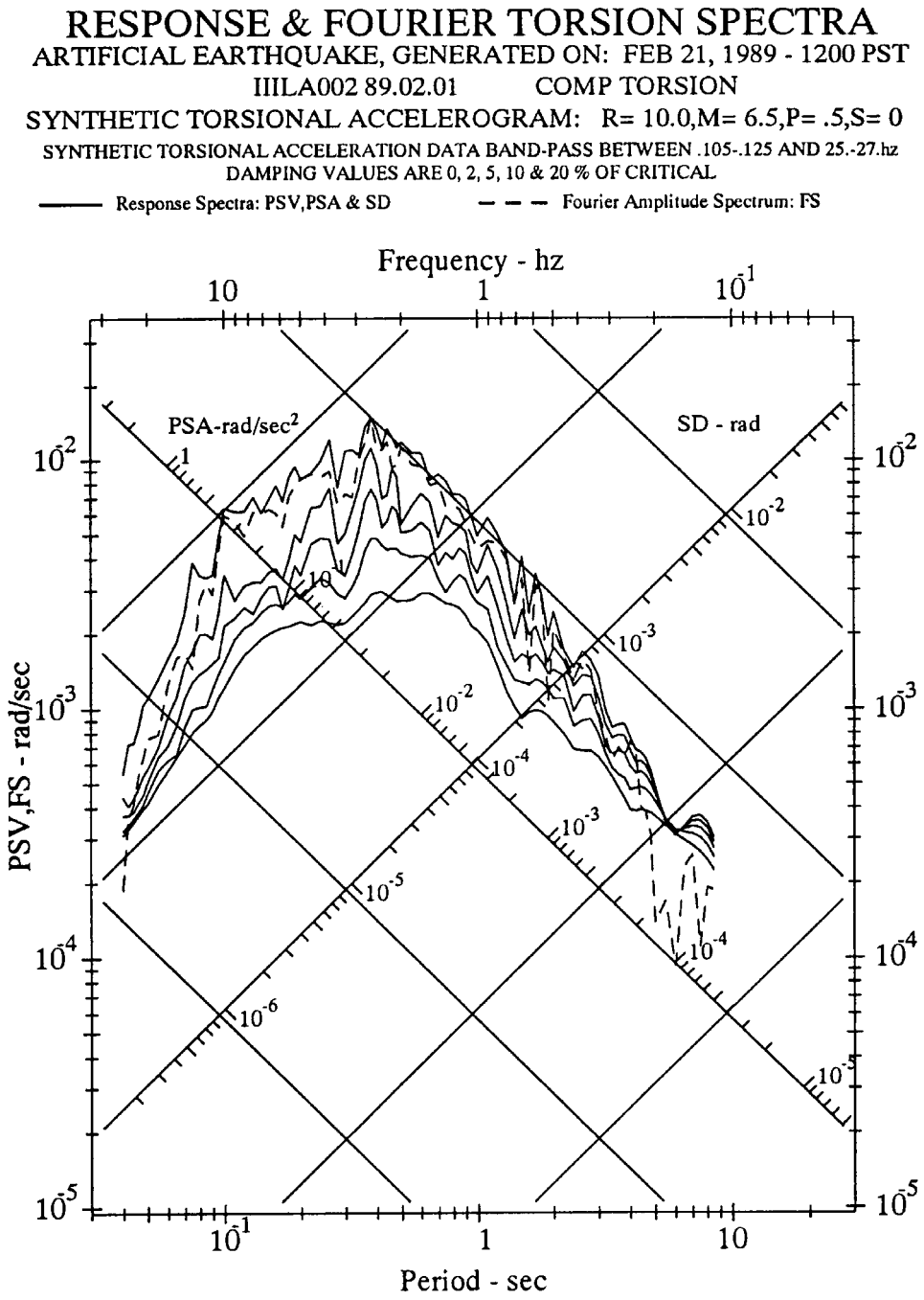

Fig. 7 Artificial earthquake synthetic torsional response and Fourier spectra

THE ROCKING COMPONENT OF STRONG EARTHQUAKE GROUND MOTION

The rotational components of strong earthquake ground motions have been studied by a number of investigators since the 1970's (Lee, 1979; Trifunac, 1982). Yim et al. (1980), and Koh and Spanos (1984) studied the rocking response of rigid structures to strong ground motion. Ishiyama (1982) investigated the motions and overturning of a rigid body in response to earthquake excitations, both experimentally and theoretically. Psycharis (1983) studied the rocking, toppling and uplift of flexible structures due to earthquake motions. Similar studies were carried out by Kato et al. (1984), and by Baba and Nakashima (1984).

As in the case of torsional motions, the development of strong-motion instruments to record the rocking components of earthquake ground motions is slow. It is again necessary to estimate these motions in terms of the corresponding translational components of strong shaking. For this purpose, the earlier work of Trifunac (1982) on calculating the rocking angles associated with incident plane P- and SV-waves was extended by Lee and Trifunac (1987) to calculate the rocking component of motion associated with incoming P-, SV- and Rayleigh waves.

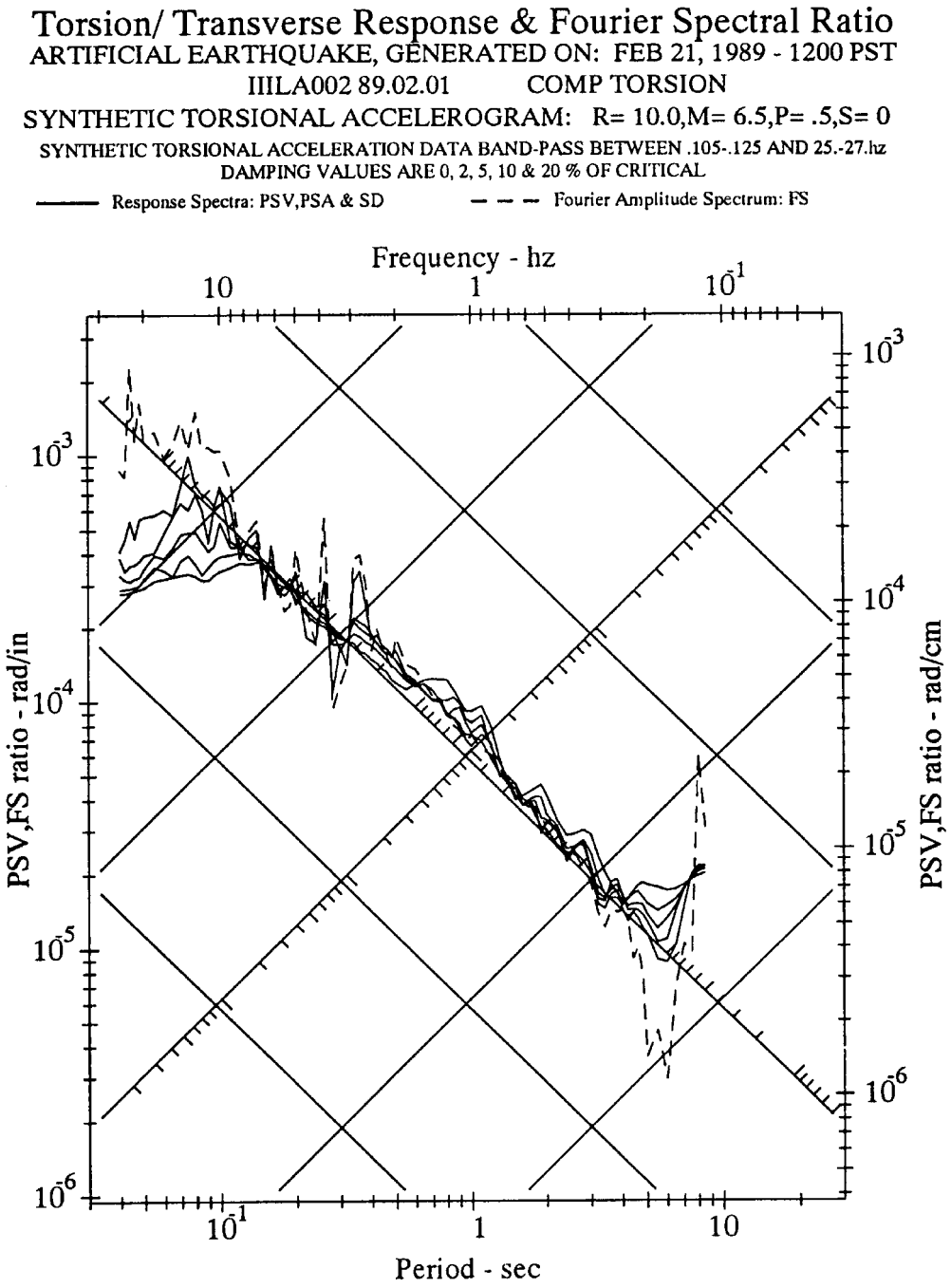

Fig. 8 Artificial earthquake synthetic torsion/transverse response and Fourier spectral ratio

1. The Rocking Motion Associated with Incident Waves

The following describes estimation of the rocking component from the known translational components of motion. Estimating the rocking from incident P- and SV-waves has been reviewed by Trifunac (1982).

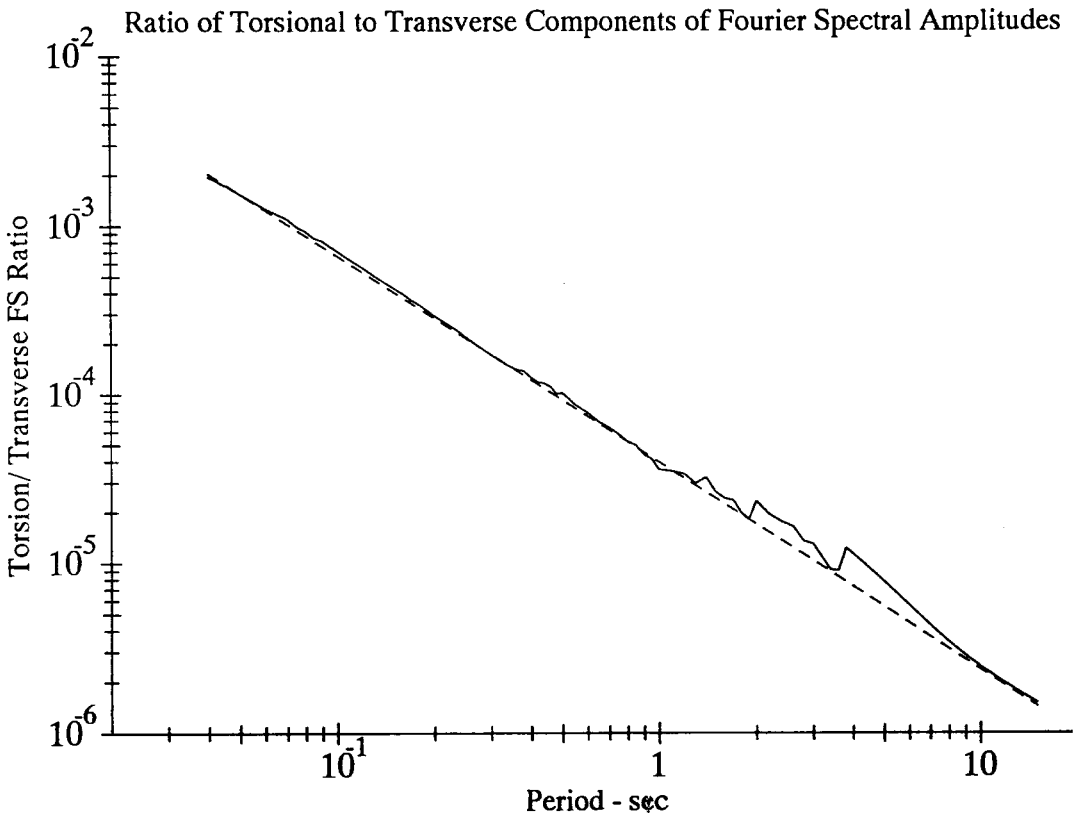

Fig. 9 Artificial earthquake synthetic torsion/transverse Fourier spectral ratio

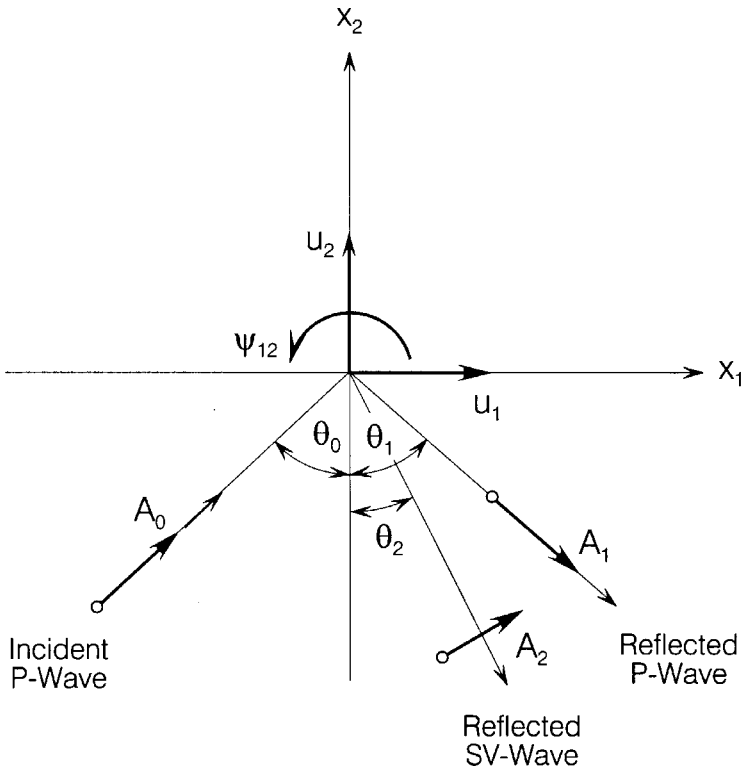

Fig. 10 Incident P-wave on half-space

1.1 Incident P-Waves

Figure 10 shows the coordinate system (x_1, x_2) and the incident and reflected rays associated with incident plane P-waves in an elastic homogeneous and isotropic half-space $(x_2 \le 0)$. The amplitudes of the incident and reflected P-waves, and reflected SV-waves are A_0, A_1, and A_2, respectively. Two components of motion at the surface $(x_2 = 0)$ are

$$u_1 = \left(A_0 \sin\theta_0 + A_1 \sin\theta_1 + A_2 \cos\theta_2\right) \exp\left[i\left(k_\alpha x_1 \sin\theta_0 - \omega t\right)\right] \tag{26}$$

$$u_2 = \left(A_0 \cos\theta_0 - A_1 \cos\theta_1 + A_2 \sin\theta_2\right) \exp\left[i\left(k_\alpha x_1 \sin\theta_0 - \omega t\right)\right] \tag{27}$$

and the rocking component about the x_3 – direction is given by

$$\psi_{12} = \frac{1}{2}\left(\frac{\partial u_2}{\partial x_1} - \frac{\partial u_1}{\partial x_2}\right) = \frac{i}{2} A_2 k_\beta \exp\left[i\left(k_\alpha x_1 \sin\theta_0 - \omega t\right)\right] \tag{28}$$

where, k_α and k_β are

$$k_\alpha = \omega/\alpha, \quad k_\beta = \omega/\beta \tag{29}$$

with ω being the circular frequency, and α and β, the respective velocities of P- and SV-waves. In the above and subsequent equations, t represents time and $i \equiv \sqrt{-1}$. Trifunac (1982) further showed that

$$\left|\psi_{12}/u_2\right| = \left(\beta/\alpha\right)\left(\omega/C_\alpha\right) \tag{30}$$

thus expressing rocking in terms of the translation, u_2. Here, C_α is the horizontal phase velocity.

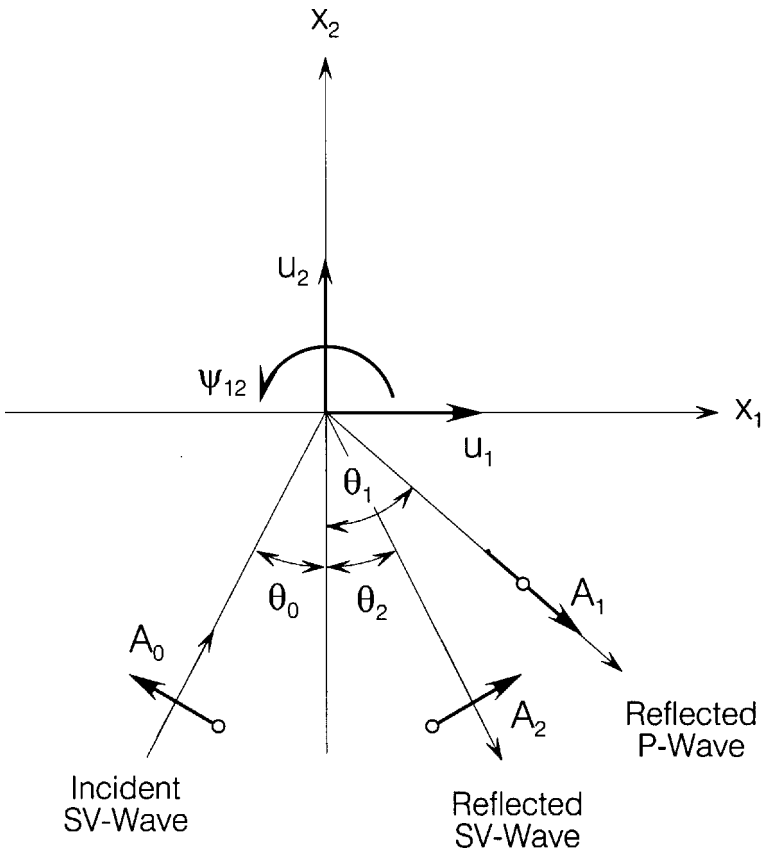

Fig. 11 Incident SV-wave on half-space

1.2 Incident SV-Waves

Figure 11 shows the coordinate system (x_1, x_2) and the incident and reflected rays associated with plane SV-waves. The amplitudes of the incident SV-waves and reflected P- and SV-waves are A_0, A_1 and A_2, respectively. The two translational, u_1 and u_2, and rocking, ψ_{12}, components of motions are

$$u_1 = \left(-A_0 \cos\theta_0 + A_1 \sin\theta_1 + A_2 \cos\theta_2\right) \exp\left[i\left(k_\beta x_1 \sin\theta_0 - \omega t\right)\right] \tag{31a}$$

$$u_2 = \left(A_0 \sin\theta_0 - A_1 \cos\theta_1 + A_2 \sin\theta_2\right) \exp\left[i\left(k_\beta x_1 \sin\theta_0 - \omega t\right)\right] \tag{31b}$$

and

$$\psi_{12} = \frac{1}{2}\left(\frac{\partial u_2}{\partial x_1} - \frac{\partial u_1}{\partial x_2}\right) = \frac{ik_\beta}{2}\left(A_0 + A_2\right) \exp\left[i\left(k_\beta x_1 \sin\theta_0 - \omega t\right)\right] \tag{32}$$

The ratio,

$$\left|\psi_{12}/u_2\right| = \omega/C_\alpha \tag{33}$$

gives the rocking component ψ_{12} in terms of the translational component u_2.

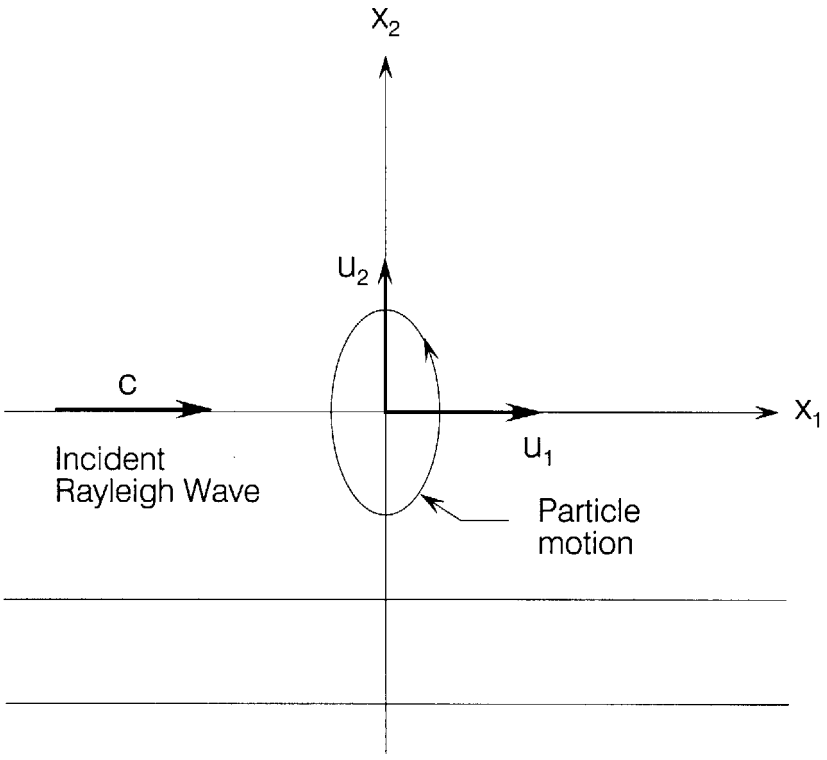

Fig. 12 Incident Rayleigh wave on half-space

1.3 Rayleigh Waves

Figure 12 shows the coordinate system (x_1, x_2) for the half-space with L layers, with the last (L-th) layer extending to $x_2 = -\infty$. Using Lamé potentials, Φ and Ψ, the Rayleigh waves in the top layer are given by

$$\Phi = \left[A_1 \exp(ikrx_2) + A_2 \exp(-ikrx_2)\right]\exp\left(ik\left(x_1 - ct\right)\right) \tag{34a}$$

and

$$\Psi = \left[B_1 \exp(iksx_2) + B_2 \exp(-iksx_2)\right]\exp\left(ik\left(x_1 - ct\right)\right) \tag{34b}$$

where, $k = \omega/c$ is the wave number, c is the phase velocity in the x_1 – direction, A_1, A_2, B_1 and B_2, are the amplitudes to be determined, and r and s are defined by

$$r^2 = \left(c^2/\alpha^2 - 1\right) \tag{35a}$$

$$s^2 = \left(c^2/\beta^2 - 1\right) \tag{35b}$$

The two components of displacement are given by

$$u_1 = \frac{\partial \Phi}{\partial x_1} + \frac{\partial \Psi}{\partial x_2} \tag{36a}$$

and

$$u_2 = \frac{\partial \Phi}{\partial x_2} - \frac{\partial \Psi}{\partial x_1} \tag{36b}$$

Using Equations (34a) and (34b), this gives

$$u_1 = ik\left[A_1 \exp\left(ikrx_2\right) + A_2 \exp\left(-ikrx_2\right) + sB_1 \exp\left(iksx_2\right) - sB_2 \exp\left(-iksx_2\right)\right]\exp\left(ik\left(x_1 - ct\right)\right) \tag{37a}$$

and

$$u_2 = ik\left[rA_1 \exp\left(ikrx_2\right) - rA_2 \exp\left(-ikrx_2\right) + B_1 \exp\left(iksx_2\right) - B_2 \exp\left(-iksx_2\right)\right]\exp\left(ik\left(x_1 - ct\right)\right) \tag{37b}$$

From

$$\frac{\partial u_1}{\partial x_2} = -k^2\left[rA_1 \exp\left(ikrx_2\right) - rA_2 \exp\left(-ikr_2\right) + s^2 B_1 \exp\left(iksx_2\right) + s^2 B_2 \exp\left(-iksx_2\right)\right]* \exp\left(ik\left(x_1 - ct\right)\right) \tag{38a}$$

and

$$\frac{\partial u_2}{\partial x_1} = -k^2\left[rA_1 \exp\left(ikrx_2\right) - rA_2 \exp\left(-ikrx_2\right) - B_1 \exp\left(iksx_2\right) - B_2 \exp\left(-iksx_2\right)\right]* \exp\left(ik\left(x_1 - ct\right)\right) \tag{38b}$$

the rocking component is

$$\psi_{12} = \frac{1}{2}\left(\frac{\partial u_2}{\partial x_1} - \frac{\partial u_1}{\partial x_2}\right) = \frac{k^2\left(1 + s^2\right)}{2} \times \left[B_1 \exp\left(iksx_2\right) + B_2 \exp\left(-iksx_2\right)\right]\exp\left(ik\left(x_1 - ct\right)\right) \tag{39}$$

At the surface of the half-space $\left(x_2 = 0\right)$, this reduces to

$$\psi_{12} = \frac{k^2\left(1 + s^2\right)}{2}\left(B_1 + B_2\right)\exp\left(ik\left(x_1 - ct\right)\right) \tag{40}$$

Equation (40) can be simplified further. The potentials Φ and Ψ in Equation (34) also satisfy the stress-free boundary conditions at the surface of the half-space $\left(x_2 = 0\right)$:

$$\sigma_{22} = \sigma_{12} = 0 \tag{41}$$

where, σ_{22} is the normal stress, and σ_{12} is the shear stress. Those are given by

$$\sigma_{22} = \lambda\Delta^2\Phi + 2\mu\frac{\partial^2 \Phi}{\partial x_2^2} - 2\mu\frac{\partial^2 \Psi}{\partial x_1 \partial x_2} \tag{42a}$$

and

$$\sigma_{12} = 2\mu\frac{\partial^2 \Phi}{\partial x_1 \partial x_2} + \mu\left(\frac{\partial^2 \Phi}{\partial x_2^2} - \frac{\partial^2 \Psi}{\partial x_1^2}\right) \tag{42b}$$

with λ and μ being the Lamé constants. Using the expressions for Φ and Ψ in Equation (34) to calculate σ_{12} and setting it to zero at $x_2 = 0$ gives

$$-2r(A_1 - A_2) + (1 - s^2)(B_1 + B_2) = 0 \tag{43}$$

Also, from Equation (37), the displacement u_2 at $x_2 = 0$ is

$$u_2\big|_{x_2=0} = ik\left(r(A_1 - A_2) - (B_1 + B_2)\right) \tag{44}$$

Combining Equations (43) and (44) gives

$$u_2\Big|_{x_2=0} = \frac{-ik}{2}(1 + s^2)(B_1 + B_2)\exp(ik(x_1 - ct)) \tag{45}$$

from which the rocking at the surface $(x_2 = 0)$ is (see Equation (40)):

$$\psi_{12} = iku_2 = i\omega u_2 / c \tag{46}$$

This is a very simple result, as in the case of incident P-waves (Equation (30)) or incident SV-waves (Equation (33)). Equation (46) will be used in conjunction with our method for the synthesis of artificial translational accelerograms to construct the time-history of rocking.

The simple relations between rocking ψ_{12} and displacement u_2 in all of the above three cases (plane P-, SV-waves, and surface Rayleigh waves) is a consequence of a more fundamental principle satisfied by elastic waves in general. Starting with the Φ and Ψ potentials, the two components of displacement, u_1 and u_2, are given by Equation (36). At the surface of the half space $(x_2 = 0)$, the boundary condition $\sigma_{12} = 0$ implies that (Equation (42))

$$2\frac{\partial^2 \Phi}{\partial x_1 \partial x_2} + \frac{\partial^2 \Psi}{\partial x_2^2} - \frac{\partial^2 \Psi}{\partial x_1^2} = 0 \tag{47a}$$

or

$$\frac{\partial}{\partial x_2}\left(\frac{\partial \Phi}{\partial x_1} + \frac{\partial \Psi}{\partial x_2}\right) + \frac{\partial}{\partial x_1}\left(\frac{\partial \Phi}{\partial x_2} - \frac{\partial \Psi}{\partial x_1}\right) = 0 \tag{47b}$$

so that Equation (36) shows that this is equivalent to

$$\left(\frac{\partial u_1}{\partial x_2} + \frac{\partial u_2}{\partial x_1}\right)\Big|_{x_2=0} = 0 \tag{48}$$

The rocking ψ_{12} at the surface $(x_2 = 0)$ then becomes

$$\psi_{12} = \frac{1}{2}\left(\frac{\partial u_2}{\partial x_1} - \frac{\partial u_1}{\partial x_2}\right) = \frac{\partial u_2}{\partial x_1} = -\frac{\partial u_1}{\partial x_2} \tag{49}$$

Thus, if the waves have the displacement u_2 given by

$$u_2 = f(x_2)\exp(ik(x_1 - ct)) \tag{50}$$

for a general function $f(x_2)$, such that the wave equations are satisfied, then from Equation (49)

$$\psi_{12} = iku_2 \tag{51}$$

which is the simple relation previously obtained for all three cases. Similar conclusion can be drawn for the torsional motions also.

2. Estimation of Synthetic Rocking

From the preceding analysis, it is seen that the rocking component of motion, ψ_{12}, can be related to the translational component, u_2, of the Rayleigh surface waves in the layered half-space. Equation (46) further shows that at the ground surface $(x_2 = 0)$, the amplitudes of rocking increase linearly with frequency ω. Similar results have been previously observed for the case of torsional motion, where it

was shown that the torsional component of motion, ψ_{13}, is associated with the translational component, u_3, of the Love waves at $x_2 = 0$

$$\Psi_{13} = \frac{-i}{2} k u_3 = -\frac{i}{2}\frac{\omega}{c} u_3 \tag{52}$$

where, c is the phase velocity of Love waves. The same estimation steps can thus be carried over from torsion to rocking. Starting from the $m-$th mode of surface waves within the frequency band $\omega_n \pm \Delta\omega_n$, the Fourier transform of the vertical translation, $\mathsf{A}_{nm}(\omega)$, is given by (Lee and Trifunac, 1987)

$$\mathsf{A}_{nm}(\omega) = \begin{cases} \pi \big/ 2 A_{nm} e^{-i\left[(\omega-\omega_n)t^*_{nm}+\phi_n\right]} & |\omega-\omega_n| \le \Delta\omega_n \\ 0 & \text{otherwise} \end{cases} \tag{53a}$$

and

$$\mathsf{A}_{nm}(-\omega) = \mathsf{A}^*_{nm}(\omega) \tag{53b}$$

where, $\mathsf{A}^*_{nm}(\omega)$ is the complex conjugate of $\mathsf{A}_{nm}(\omega)$. A_{nm} is the relative amplitude of the $m-$th mode, given by the empirical equations suggested by Trifunac (1971b), and has been used in the synthesis of artificial accelerograms for both the translational components and torsional component. t^*_{nm} is the arrival time of the $m-$th mode defined earlier. ϕ_n is the phase of the wave at the given frequency band, introduced to include the effects of source and other miscellaneous effects along the propagation path. It is assumed to be a random number between $-\pi$ and π.

The corresponding Fourier transform of the $m-$th mode of rocking, $\Psi_{nm}(\omega)$, in the frequency band, $2\Delta\omega_n$, is

$$\Psi_{nm}(\omega) = \begin{cases} \left(i\pi\omega/2C_{nm}\right) A_{nm} e^{-i\left[(\omega-\omega_n)t^*_{nm}+\phi_n\right]} & |\omega-\omega_n| \le \Delta\omega_n \\ 0 & \text{otherwise} \end{cases} \tag{54}$$

where, $C_{nm} = C_{nm}(\omega_n)$ is the phase velocity of the $m-$th mode of Rayleigh waves, assumed to be constant within the frequency band $\omega_n \pm \Delta\omega_n$. Combining all of the *M* modes of Rayleigh waves gives the Fourier transform of vertical displacement, $\mathsf{A}_n(\omega)$, at the frequency band as

$$\mathsf{A}_n(\omega) = \sum_{m=1}^{M} \mathsf{A}_{nm}(\omega) \tag{55}$$

Note that for the Fourier transform of horizontal displacements, this will include both the modes of Love and Rayleigh waves in the band $2\Delta\omega_n$, and with relative contributions determined from the angles between x_1 and x_3 axes relative to the azimuth of wave arrival. Similarly, the total rocking, $\Psi_n(\omega)$, at the frequency band $2\Delta\omega_n$ is

$$\Psi_n(\omega) = \sum_{m=1}^{M} \psi_{nm}(\omega) \tag{56}$$

The total Fourier transforms of vertical displacement, $\mathsf{A}(\omega)$, and rocking, $\Psi(\omega)$, then become

$$\mathsf{A}(\omega) = \sum_{n=1}^{N} \alpha_n \mathsf{A}_n(\omega) \tag{57a}$$

and

$$\Psi(\omega) = \sum_{n=1}^{N} \alpha_n \Psi_n(\omega) \tag{57b}$$

where, N is the total number of frequency bands considered. α_n is the scaling factor determined so that the Fourier amplitude of vertical displacement at frequency ω_n will match with the corresponding actual or estimated component of Fourier amplitude $|FS(\omega_n)|$ at the site. The actual Fourier amplitudes are those calculated from the actual accelerogram recorded at the site. The estimated Fourier amplitudes are those calculated from the empirical models for scaling Fourier amplitude spectra of strong ground acceleration in terms of the earthquake magnitude, source-to-station distance, site intensity, and recording site conditions.

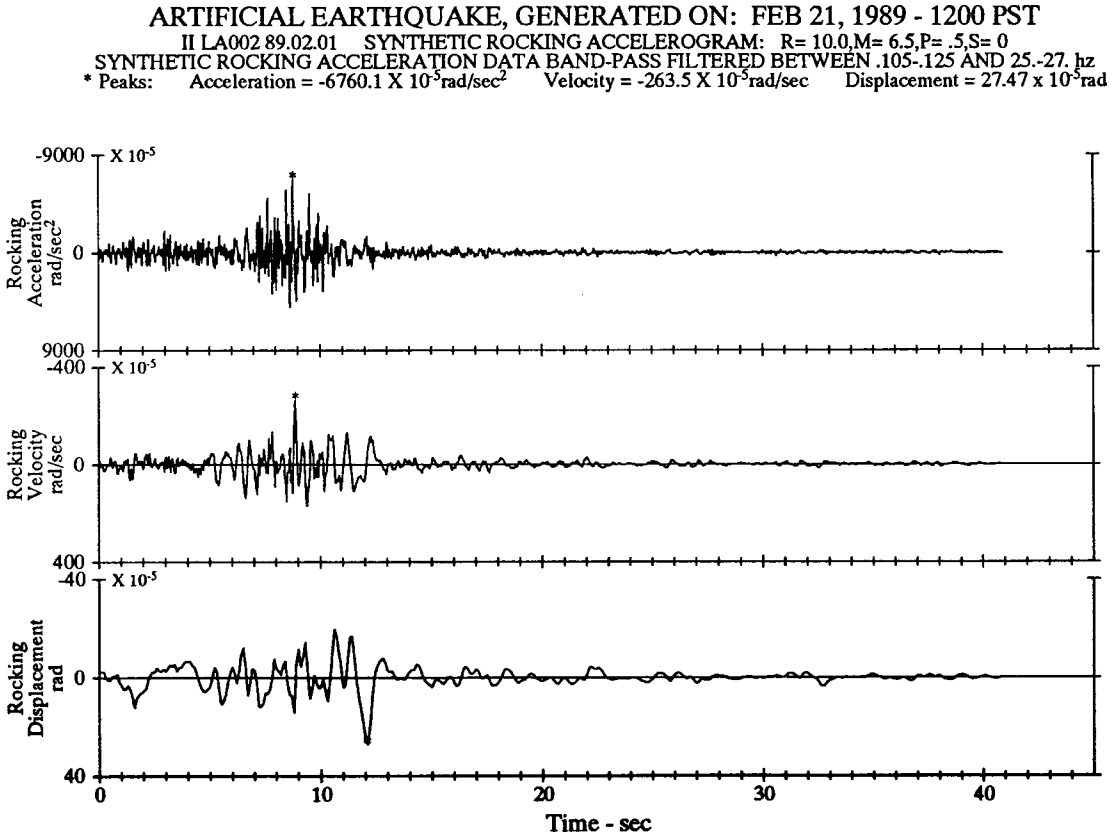

Fig. 13 Artificial earthquake synthetic rocking accelerogram

The ratio of the Fourier amplitude of rocking acceleration to that of vertical translation is

$$\left|\frac{\Psi(\omega)}{\mathsf{A}(\omega)}\right| \cong \left|\frac{\Psi_n(\omega)}{\mathsf{A}_n(\omega)}\right|, \quad |\omega - \omega_n| \le \Delta\omega_n \tag{58}$$

Using Equations (53) through (56), this becomes

$$\left|\frac{\Psi(\omega)}{\mathsf{A}(\omega)}\right| = \omega \left| \frac{\sum_{m=1}^{M} \frac{A_{nm}}{C_{nm}} e^{-i(\omega-\omega_n)t^*_{nm}}}{\sum_{m=1}^{M} A_{nm} e^{-i(\omega-\omega_n)t^*_{nm}}} \right|, \quad |\omega - \omega_n| \le \Delta\omega_n \tag{59}$$

and, in particular for $\omega = \omega_n$,

$$\left|\frac{\Psi(\omega)}{\mathsf{A}(\omega)}\right| = \omega_n \left| \frac{\sum_{m=1}^{M} A_{nm}/C_{nm}}{\sum_{m=1}^{M} A_{nm}} \right| \tag{60}$$

Note that except for the factor of 1/2, the same empirical relation was obtained for the ratio of Fourier amplitude of torsional to Fourier amplitude of horizontal accelerations.

As for torsional motions, the asymptotic expansion of Equation (60) for large and small frequencies is possible here. At the high-frequency end, the phase velocities of all modes of Rayleigh surface waves approach $\beta_{\min}$, the minimum shear wave velocity in the layered half-space model. Thus,

$$\left|\frac{\Psi(\omega_n)}{\mathsf{A}(\omega_n)}\right| \sim \omega_n \frac{\sum_{m=1}^{M} A_{nm}/\beta_{\min}}{\sum_{m=1}^{M} A_{nm}} = \frac{\omega_n}{\beta_{\min}} \qquad \text{as } \omega_n \to \infty \tag{61}$$

At the low-frequency end, the only mode present in the layered medium is the first mode, and its phase velocity approaches $\beta_{\max}$, the largest (usually for half-space) shear wave velocity in the layered model. Thus,

$$\left|\frac{\Psi(\omega_n)}{\mathsf{A}(\omega_n)}\right| \sim \omega_n \left|\frac{A_{n1}/\beta_{\max}}{A_{n1}}\right| = \omega_n/\beta_{\max} \qquad \text{as } \omega_n \to \infty \tag{62}$$

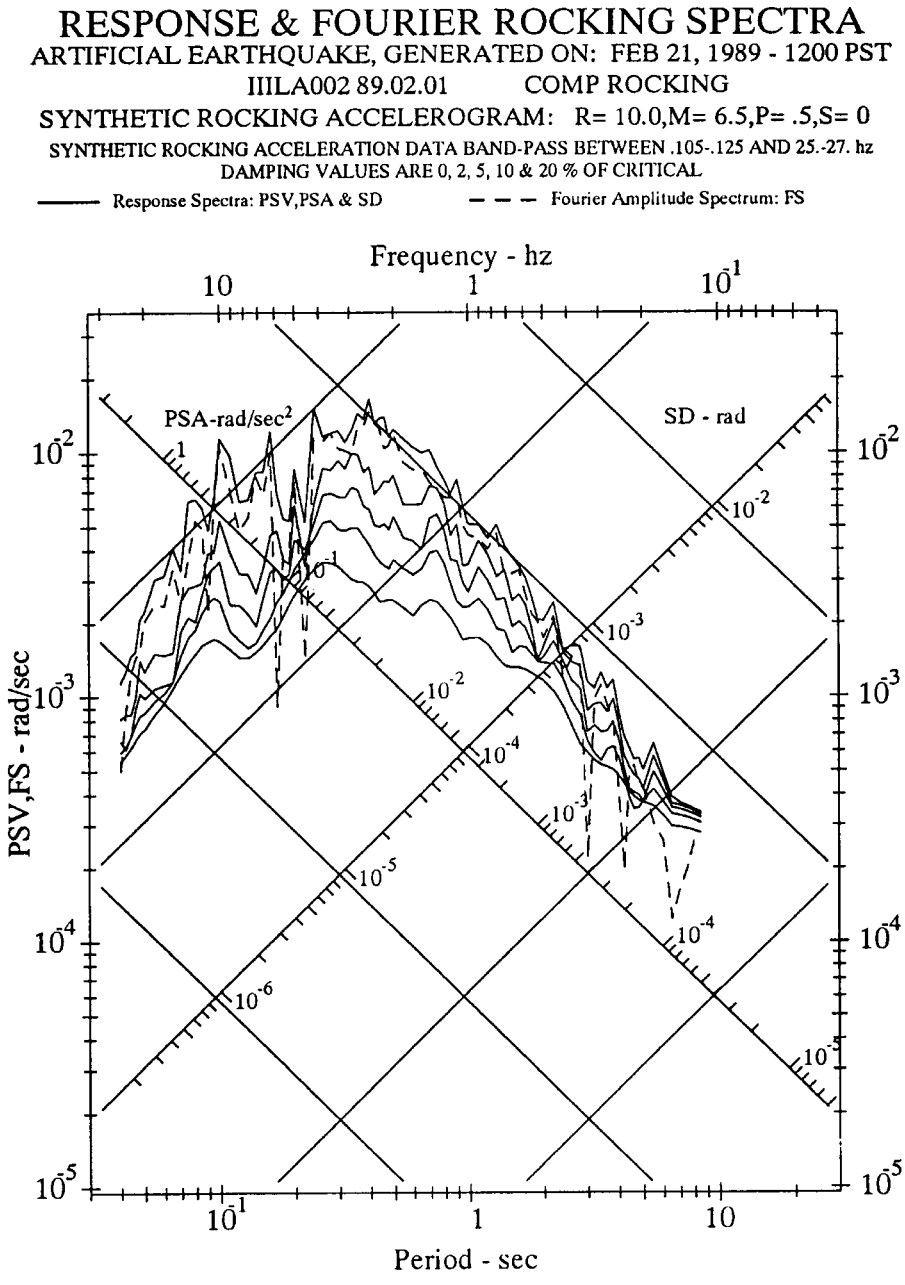

Fig. 14 Artificial earthquake synthetic rocking response and Fourier spectra

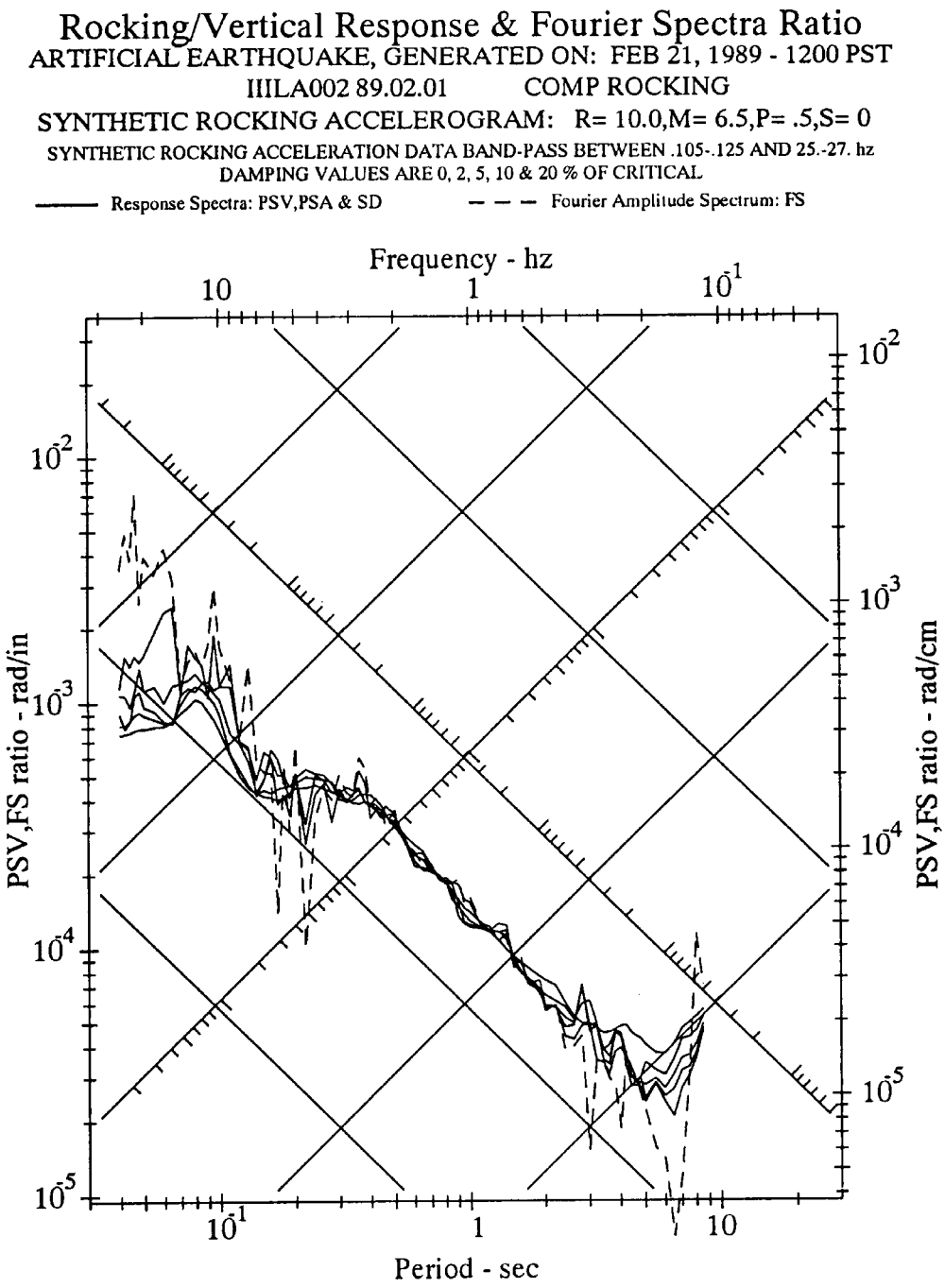

Fig. 15 Artificial earthquake synthetic rocking/vertical response and Fourier spectral ratio

3. Examples of Synthetic Rocking

Following the analysis in the previous sections, one can readily generate the translational (horizontal: radial, transverse; and vertical), torsional and rocking accelerograms simultaneously. As in Sub-section 3 of the previous section, the same site at Westmoreland in Imperial Valley, and the same dispersion curves are used in the following examples.

Figure 13 shows a plot of the synthetic rocking motions. It presents examples of the rocking acceleration, velocity and displacement in rad/s^2, rad/s, and rad, respectively. Figure 14 gives the corresponding rocking response and Fourier spectra. It represents the maximum rocking responses of over 80 single-degree-of-freedom systems, with natural periods in the range 0.04-8 s and with 5 damping ratios $(\zeta = 0,\ 0.02,\ 0.05,\ 0.10 \text{ and } 0.20)$, when subjected to the corresponding rocking accelerograms. The units for the rocking displacement, SD, pseudo relative velocity, PSV, and pseudo acceleration, PSA, responses are rad, rad/s, and rad/s^2, respectively. Figure 15 shows the ratio of rocking to vertical

translational response. As indicated in Equation (46), this ratio tends to vary linearly with frequency, or inversely with period.

SURFACE STRAINS OF EARTHQUAKE GROUND MOTIONS

Expressions for surface strains in an elastic half-space associated with incident plane (P, SV and SH) body waves are given in Trifunac (1979b). Those associated with the Rayleigh and Love surface waves are given in Lee (1990).

Studies of earthquake-induced damage to engineered structures show that there are cases of damages, which result from the differential motions caused by large strains associated with ground shaking (Trifunac, 1979b, 1997). In some cases, these strains are superimposed on the dynamic responses, and only contribute to the resultant total vibrations. In other cases, when the characteristic frequencies of the system differ from the principal frequency content of strong motion, these local strains may affect the structural systems in a quasi-static manner. Long underground pipelines and railroad tracks may buckle, and bridges may collapse because of the excessive differential support motions, due to excessive local strains associated with earthquake ground shaking (Trifunac and Todorovska, 1997a, 1997b; Trifunac et al., 1996). Studies of the responses of long structures excited by ground shaking (Kojić et al., 1988; Todorovska and Trifunac, 1989, 1990a, 1990b; Trifunac and Todorovska, 1997a) have demonstrated the need for detailed description of motions at various points of single (or multiple) foundation(s), with emphasis on the differential motions associated with large surface strains.

1. The Surface Strains Associated with Incident Waves

This sub-section is devoted to estimation of the surface strains from the known translational components of motion (Trifunac, 1979b; Lee, 1990). Referring to Figures 10 and 11 for incident P- and SV-waves, and Figure 5 for incident SH-waves, the surface strains at $x_2 = 0,$ associated with incident P- and SV-waves, are

$$\varepsilon_{x_1} = u_{1,1} = ik_\alpha \sin\theta_0 u_1 \tag{63a}$$

$$\varepsilon_{x_2} = u_{2,2} = ik_\alpha \left(\frac{2}{(\alpha/\beta)^2} - 1 \right) \sin\theta_0 u_1 \tag{63b}$$

and

$$\varepsilon_{x_1 x_2} = 1/2\left(u_{1,2} + u_{2,1}\right) = 0 \tag{63c}$$

Those associated with incident plane SH-waves are

$$\varepsilon_{x_1} = \varepsilon_{x_2} = 0 \tag{64a}$$

$$\varepsilon_{x_1 x_3} = 1/2\left(u_{1,3} + u_{3,1}\right) = (1/2)u_{3,1} = (1/2)ik_\beta \sin\theta_0 u_3 \tag{64b}$$

Lee (1990) showed that similar expressions for surface strains can also be derived for the Rayleigh and Love waves. Referring to Equations (34)-(37) for the Φ and Ψ potentials, and the horizontal (x_1) and vertical (x_2) components of displacements associated with Rayleigh waves, the associated surface strains at $x_2 = 0$ are

$$\varepsilon_{x_1} = u_{1,1} = -k^2\left[A_1 + A_2 + s(B_1 - B_2)\right]\exp\left(ik(x_1 - ct)\right) \tag{65a}$$

$$\varepsilon_{x_2} = u_{2,2} = -k^2\left[r(A_1 + A_2) - s(B_1 - B_2)\right]\exp\left(ik(x_1 - ct)\right) \tag{65b}$$

where, $c(< \beta < \alpha)$ is the phase velocity of the surface waves in the $x_1 -$direction; $k = \omega/c$ is the corresponding wave number; and r and s are, respectively, numbers given by (Equation (35))

$$r = \left(c^2/\alpha^2 - 1\right)^{1/2} \tag{66a}$$

$$s = \left(c^2/\beta^2 - 1\right)^{1/2} \tag{66b}$$

Recall from Equation (37a) that the horizontal component of displacement at the surface $(x_2 = 0)$ is given by

$$u_1 = ik\left[A_1 + A_2 + s(B_1 - B_2)\right]\exp(ik(x_1 - ct)) \tag{67}$$

It is clear from Equations (65a) and (67) that for Rayleigh waves, the surface normal strain in the horizontal (x_1) direction at $x_2 = 0$ is

$$\varepsilon_{x_1} = u_{1,1} = iku_1 \tag{68}$$

The surface normal strain, ε_{x_2}, in the vertical (x_2) direction at $x_2 = 0$ can also be expressed in terms of u_1. Recalling the stress-free boundary conditions at the half-space surface (Equation (41)),

$$\sigma_{22} = \sigma_{12} = 0 \tag{69}$$

and, from Equation (42), expressing the stresses in terms of the potentials at $x_2 = 0$ gives

$$(1 - s^2)(A_1 + A_2) + 2s(B_1 - B_2) = 0 \tag{70a}$$

$$-2r(A_1 - A_2) + (1 - s^2)(B_1 + B_2) = 0 \tag{70b}$$

Using Equation (70a), Equations (67) and (65b) can be rewritten as

$$u_1 = ik\left(\frac{1 + s^2}{2}\right)(A_1 + A_2)\exp(ik(x_1 - ct)) \tag{71a}$$

$$\varepsilon_{x_2} = -k^2\left(r^2 + \frac{(1 - s^2)}{2}\right)(A_1 + A_2)\exp(ik(x_1 - ct)) \tag{71b}$$

Using the expressions for r and s in Equation (66), Equation (71) can be further simplified to

$$u_1 = ik\frac{c^2}{2\beta^2}(A_1 + A_2)\exp(ik(x_1 - ct)) \tag{72a}$$

$$\varepsilon_{x_2} = -k^2\left(c^2/\alpha^2 - c^2/2\beta^2\right)(A_1 + A_2)\exp(ik(x_1 - ct)) \tag{72b}$$

from which it follows that

$$\varepsilon_{x_2} = ik\left[\frac{2}{(\alpha/\beta)^2} - 1\right]u_1 \tag{73}$$

This is of the same form as Equation (63b), for incident plane P- and SV-waves. For $\nu = 0.25$, $(\alpha/\beta)^2 = 3$, and thus, Equation (73) takes the form

$$\varepsilon_{x_2} = -\frac{ik}{3}u_1 \tag{74}$$

The surface shear strains, $\varepsilon_{x_2x_1}$ and $\varepsilon_{x_2x_3}$, are both zero, because the corresponding shear stresses, $\tau_{x_2x_1}$ and $\tau_{x_2x_3}$, vanish at the half-space surface $(x_2 = 0)$.

Similar expressions for surface strains associated with Love waves can be derived. Starting with the anti-plane displacement, u_3, in the top layer of the layered half-space,

$$u_3 = \left(B_1 e^{iksx_2} + B_2 e^{-iksx_2}\right)\exp(ik(x_1 - ct)) \tag{75}$$

the associated surface strains are given by

$$\varepsilon_{x_1x_3} = \frac{1}{2}(u_{1,3} + u_{3,1}) = \frac{1}{2}u_{3,1} = \frac{1}{2}iku_3 \tag{76a}$$

$$\varepsilon_{x_2x_3} = \frac{1}{2}(u_{2,3} + u_{3,2}) = (1/2)u_{3,2} = 0 \tag{76b}$$

$$\varepsilon_{x_3x_3} = u_{3,3} = 0 \tag{76c}$$

The surface shear strain $\varepsilon_{x_2x_3}$ is zero, because the corresponding shear stress $\tau_{x_2x_3}$ vanishes at the half-space surface.

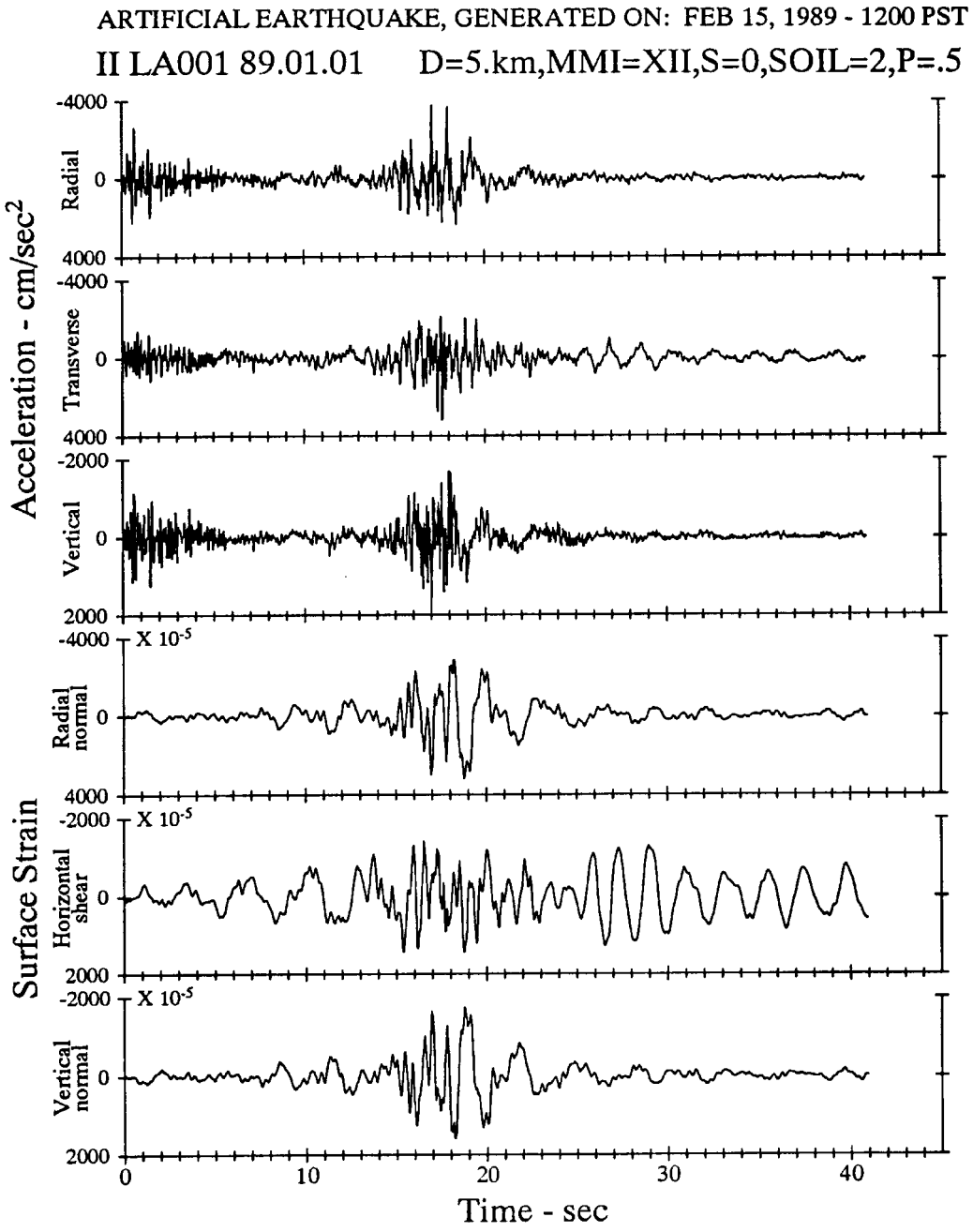

Fig. 16 Artificial earthquake synthetic acceleration and surface strain accelerogram: LA001

2. Estimation of Synthetic Strain

From the preceding analysis, it is seen that the surface strains associated with strong earthquake motions are related to the translational components of body Rayleigh and Love waves in the half-space. The three non-vanishing components of surface strains, ε_{x_1} (Equation (68)), ε_{x_2} (Equation (73)) and $\varepsilon_{x_1x_3}$ (Equation (76a)), have amplitudes, which all increase linearly with wave number k and hence with frequency ω.

From Equation (2), the $m-$th mode of acceleration of horizontal motion $\ddot{u}_1$ for Rayleigh waves has Fourier transform, within frequency band $\omega_n \pm \Delta\omega_n$, as

$$\mathsf{A}_{nm}(\omega) = \begin{cases} (\pi/2) A_{nm} e^{-i\left[(\omega-\omega_n)t^*_{nm}+\phi_n\right]} & |\omega-\omega_n| \le \Delta\omega_n \\ 0 & \text{otherwise} \end{cases}$$

and (77)

$$\mathsf{A}_{nm}(-\omega) = \mathsf{A}^*_{nm}(\omega)$$

where, $\mathsf{A}^*_{nm}(\omega)$ is the complex conjugate of $\mathsf{A}_{nm}(\omega)$. The corresponding Fourier transform of the in-plane displacement of horizontal motion, u_1, denoted by $\mathsf{U}_{nm}(\omega)$, is then

$$\mathsf{A}_{nm}(\omega) = \frac{-\mathsf{A}_{nm}(\omega)}{\omega^2} = \begin{cases} -\dfrac{\pi}{2\omega^2} A_{nm} e^{-i\left[(\omega-\omega_n)t^*_{nm}+\phi_n\right]} & |\omega-\omega_n| \le \Delta\omega_n \\ 0 & \text{otherwise} \end{cases} \quad (78)$$

Similar expressions can be written for the Fourier transform of the anti-plane displacement of horizontal motion, u_3, for Love waves. From this, on using Equations (68), (73) and (76a), the Fourier transforms of the $m-$th mode of strains $\varepsilon_{11,nm}(\omega)$, $\varepsilon_{22,nm}(\omega)$ and $\varepsilon_{13,nm}(\omega)$ (respectively for $\varepsilon_{x_1x_1}(t)$, $\varepsilon_{x_2x_2}(t)$, and $\varepsilon_{x_1x_3}(t)$), in the same frequency band $\omega_n \pm \Delta\omega_n$, become

$$\mathsf{E}_{11,nm}(\omega) = \frac{i\omega}{C_{nm}} \mathsf{U}_{nm}(\omega) = \frac{-i}{\omega C_{nm}} \mathsf{A}_{nm}(\omega) \quad (79a)$$

$$\mathsf{E}_{22,nm}(\omega) = \frac{i\omega}{C_{nm}} \left(\frac{2}{(\alpha/\beta)^2} - 1 \right) \mathsf{U}_{nm}(\omega) = \frac{-i}{\omega C_{nm}} \left(\frac{2}{(\alpha/\beta)^2} - 1 \right) \mathsf{A}_{nm}(\omega) \quad (79b)$$

$$\mathsf{E}_{13,nm}(\omega) = \frac{1}{2} \frac{i\omega}{C_{nm}} \mathsf{U}_{nm}(\omega) = \frac{-i}{2\omega C_{nm}} \mathsf{A}_{nm}(\omega) \quad (79c)$$

where, $C_{nm} = C_m(\omega_n)$ is the phase velocity of the $m-$th mode of Rayleigh waves in Equations (79a) and (79b), and $\mathsf{U}_{nm}(\omega)$ is the transform of displacement $u_1(t)$. In Equation (79c), $C_{nm} = C_m(\omega_n)$ is for the Love waves, with $\mathsf{U}_{nm}(\omega)$ being the transform of the corresponding anti-plane displacement $u_3(t)$. Those are assumed to be constant within the frequency band $\omega_n \pm \Delta\omega_n$.

As in the generation of torsion and rocking time-histories, the total contribution from all the modes of surface and body waves in the same frequency band takes the form

$$\mathsf{E}_{ij,n}(\omega) = \begin{cases} -\dfrac{i\pi}{2\omega} f_{ij} \alpha_n \sum_{m=1}^{M} A_{nm} e^{-i\left[(\omega-\omega_n)t^*_{nm}+\phi_n\right]} & |\omega-\omega_n| \le \Delta\omega_n \\ 0 & \text{otherwise} \end{cases} \quad (80)$$

where,

$$f_{ij} = \begin{cases} 1 & i = j = 1, \text{ for Rayleigh waves} \\ \dfrac{2}{(\alpha/\beta)^2} - 1 & i = j = 2, \text{ for Rayleigh waves} \\ 1/2 & i = 1,\ j = 3, \text{ for Love waves} \\ 0 & \text{otherwise} \end{cases} \quad (81)$$

and α_n is the scaling factor, as given by Equation (10). For $i = j = 1$ and $i = j = 2$, the contribution of surface waves comes only from the Rayleigh waves, and for $i = 1,\ j = 3,$ the contribution is from the Love waves. The total Fourier transform of the strain time-history is then

$$\mathrm{E}_{ij}(\omega) = \sum_{n=1}^{N} \mathrm{E}_{ij,n}(\omega) \tag{82}$$

where, N is the total number of frequency bands used.

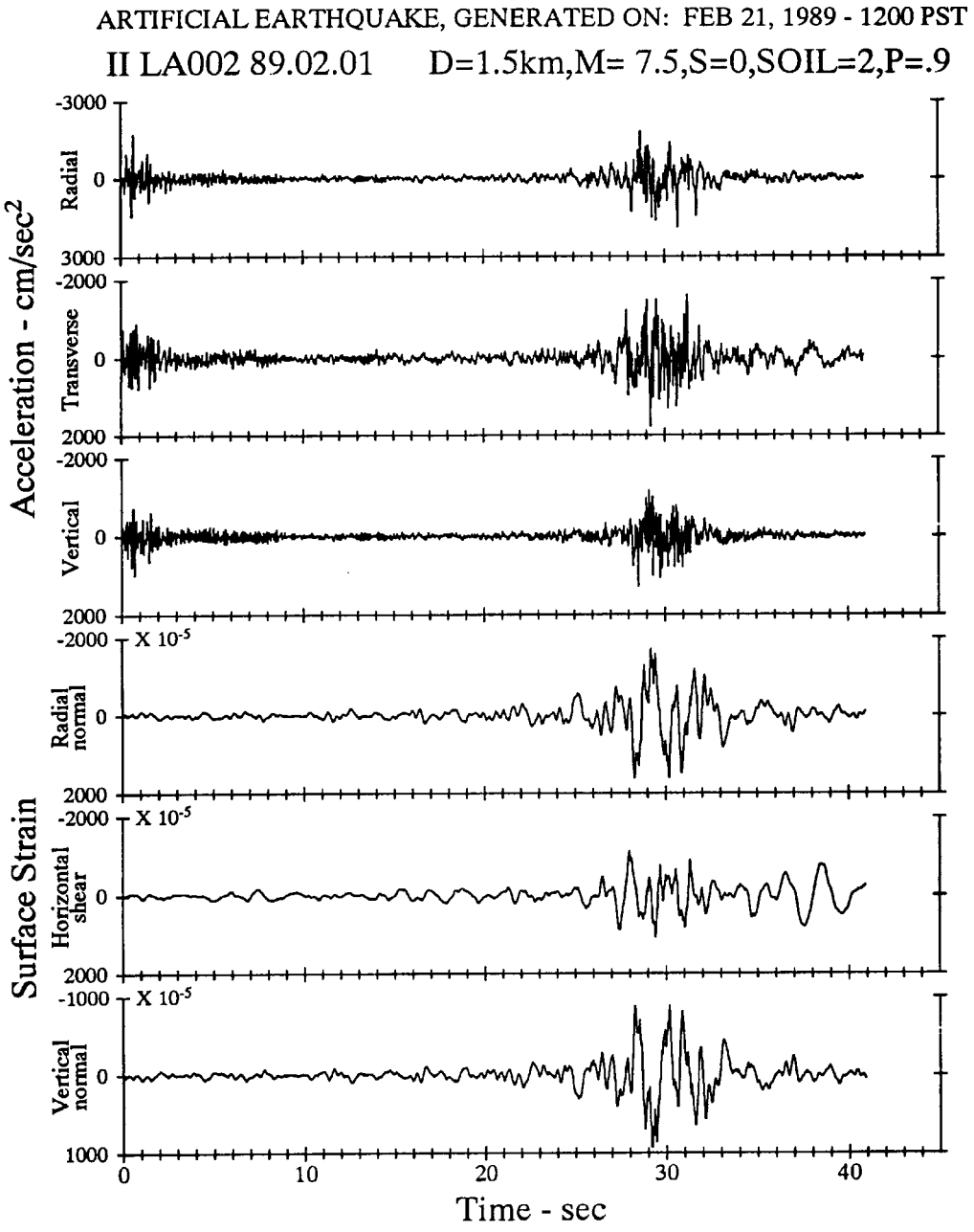

Fig. 17 Artificial earthquake synthetic acceleration and surface strain accelerogram: LA002

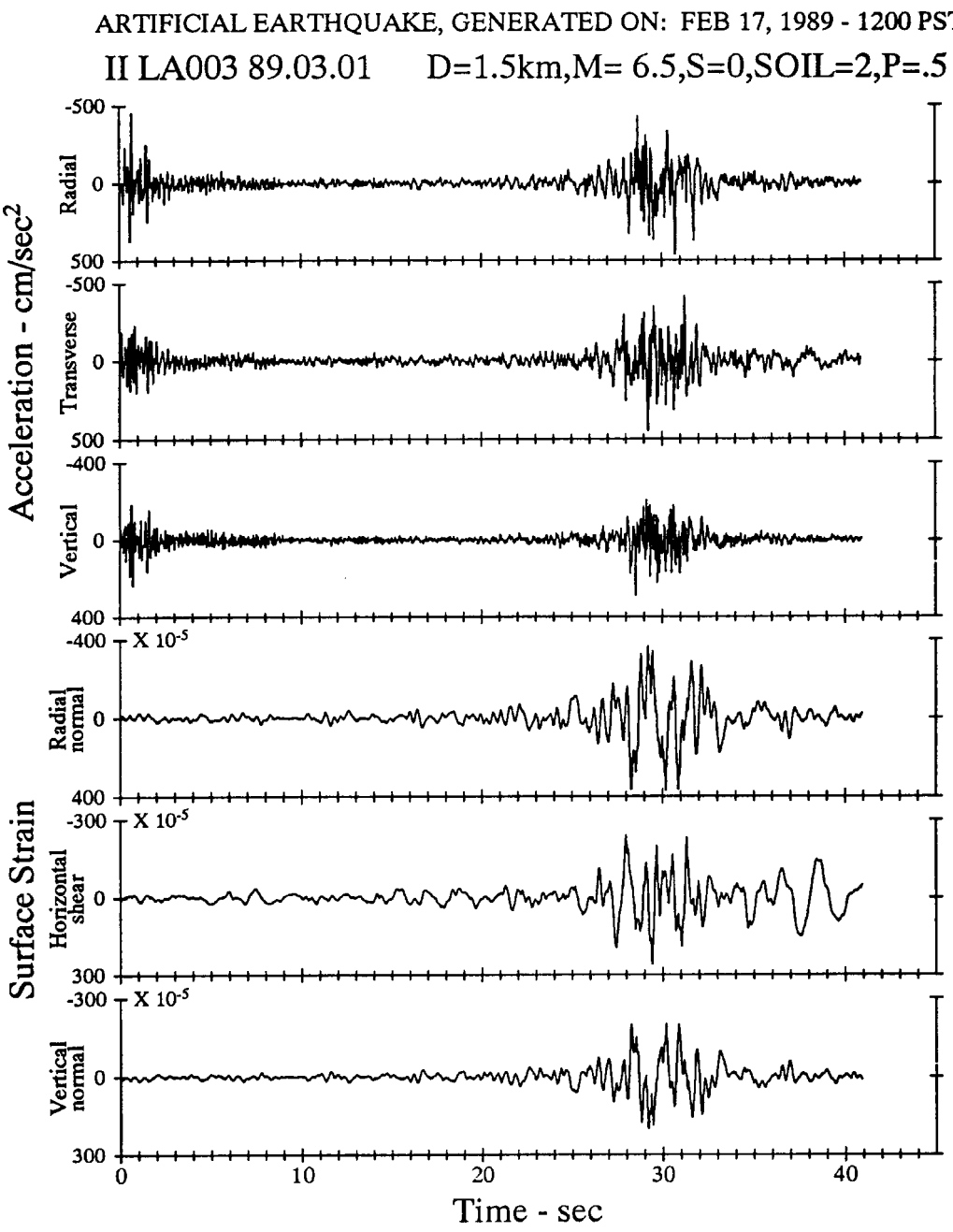

Fig. 18 Artificial earthquake synthetic acceleration and surface strain accelerogram: LA003

3. Examples of Synthetic Strains

We have earlier presented examples for the local site geology and dispersion of the surface waves for a site in Westmoreland, Imperial Valley, California. To illustrate "large" strains, we modify this "site" (see Table 2) to have a 50 m layer with shear wave velocity of 50 m/s at the top, and a second 130 m layer with shear wave velocity of 300 m/s (Table 3). For depths greater than 180 m, we adopt the material properties, as in Table 2. For long period motions, the dispersion curves for this modified model would be identical to those in Figures 1 and 2. For short periods and layer properties as in Table 3, the phase and group velocities would be reduced from 0.98 km/s to 0.05 km/s. The modified site will exemplify "soft" soil and geologic conditions in which, as implied by Equations (80) and (81), the strains can be "large". We also consider large amplitudes of strong shaking, in the immediate vicinity of the epicenter. Figure 16 presents an example computed for the site intensity, $MMI = XII$, source at epicentral distance of 5 km for $s = 0$ (site on alluvium) and $s_L = 2$ (deep soil site), and for $p = 0.5$, where p is the probability of

exceedance for the derived spectrum (Trifunac, 1989a, 1989b). These conditions result in peak accelerations (37.3 m/s^2 for radial, 31.9 m/s^2 for transverse, and 18.5 m/s^2 for vertical ground motions) larger than what has been recorded so far, and thus illustrate extreme response amplitudes and the associated strains. The resulting peak strains are, respectively, 0.03, 0.01 and 0.02. Because the strains are proportional to ku, the overall appearance of strain versus time is similar to that of the ground motion velocity. Figure 17 shows another example for M = 7.5, 1.5 km epicentral distance, $s = 0$, $s_L = 2$, and $p = 0.9$. The radial, transverse and vertical peak accelerations, respectively equal to 19.0 m/s^2, 17.86 m/s^2, and 12.9 m/s^2, lead to the corresponding peak strains equal to 0.017, 0.011, and 0.009. These examples have been chosen to illustrate the extreme cases. Considering the local geologic cross-section, as given in Table 2, M = 6.5, $s = 0$, $s_L = 2$, and $p = 0.5$ would result in peak accelerations equal to 4.59 m/s^2, 4.48 m/s^2, and 2.91 m/s^2, for example. Then, the associated strains would equal only to 3.7 x 10^{-3}, 2.6 x 10^{-3}, and 2.0 x 10^{-3}, for $\varepsilon_{x_1x_1}$, $\varepsilon_{x_1x_3}$ and $\varepsilon_{x_2x_2}$, respectively (Figure 18).

Table 3: Same as Table 2 Except for a Modification in the Top 180 m of Layer 1, to Illustrate the Effects for a "Soft" Site

Layer	h_i (km)	α (km/s)	β_i (km/s)	ρ_i (g/cm^3)
1a	0.05	0.105	0.05	1.20
1b	0.13	0.60	0.30	1.28
2	0.55	1.96	1.13	1.36
3	0.98	2.71	1.57	1.59
4	1.19	3.76	2.17	1.91
5	2.68	4.69	2.71	2.19
6	∞	6.40	3.70	2.71

The above examples illustrate the possible strain amplitudes implied by the linear theory, but those cannot be taken to be "average" or "typical" estimates, for magnitudes, site intensities, or local conditions considered. In general, the strain amplitudes will increase with overall increase in the strong motion amplitudes, and with decrease of shear wave velocities of soil and sedimentary layers near the ground surface. Time-dependence of strain components near the ground surface is roughly proportional to that of the corresponding components of ground velocity, and thus, the peak strains will also increase with the peak ground velocity.

It is seen that by using the linear theory of wave propagation, the strain amplitudes can be evaluated exactly in three-dimensions. When the local geologic conditions are too complex to model the near-surface motions by the equivalent parallel layer models, the method presented here can be modified to give again the exact representation of near-surface strains, but in terms of other than the rectangular Cartesian coordinate system (Moeen-Vaziri and Trifunac, 1988a, 1988b; Lee and Wu, 1994a, 1994b; Manoogian and Lee, 1996).

Many engineering inferences on linear and non-linear strains in rock and in soil, during the passage of seismic waves, are limited by the assumption that the incident energy arrives vertically in a one-dimensional wave propagation model. The method presented here should help in the development of input motions and input strains for modeling three-dimensional non-linear responses of soft and water-saturated soils, and for full and direct estimation of strains in the linear response range.

CURVOGRAMS OF EARTHQUAKE GROUND MOTION

Analyses of the effects of strong earthquake shaking on engineered structures are performed for dynamic forces that result from strong motion accelerations. However, pseudo-static deformations that result from wave passage under long structures may also contribute forces, which, in certain cases, may be larger than the dynamic forces (Kojić et al., 1988; Todorovska and Lee, 1989; Todorovska and Trifunac, 1989, 1990a, 1990b). Such loadings and the resulting response of structures depend on the

nature of ground waves, inhomogeneities in the soil, sediments or rock under the foundation, the surface topography near structure, and on the nature of the structure-foundation system.

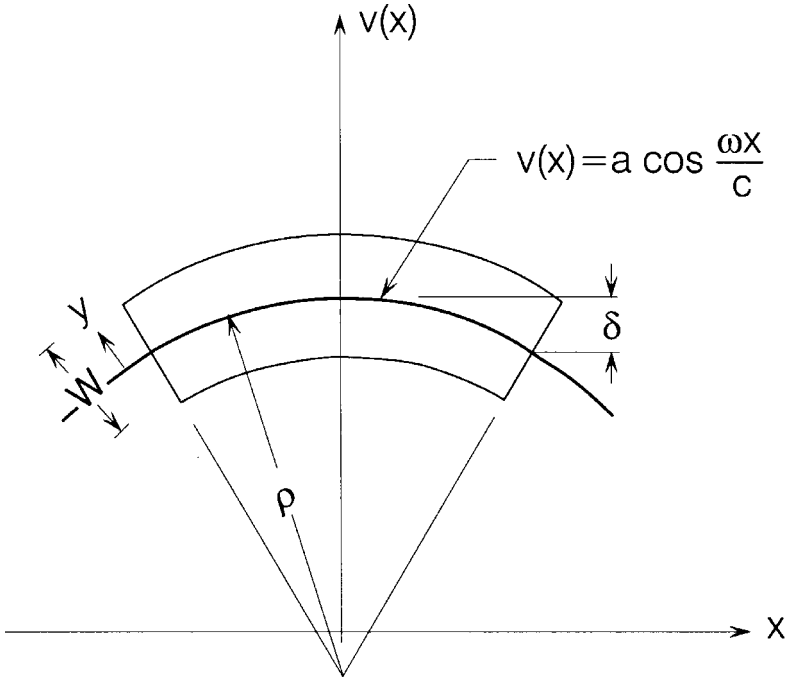

Fig. 19 Curvature

For ground waves that are long relative to the plan dimensions of a structure, it is possible to describe the strong ground motion in terms of the translational and rotational components of ground motion (Gupta and Trifunac, 1987, 1988; Lee and Trifunac, 1985, 1987; Trifunac, 1982). For short ground waves with wave lengths comparable to or shorter than the structural dimensions, the details of the wave passage analysis must be worked out to obtain realistic response analyses (Kojić et al., 1988; Todorovska and Trifunac, 1990b). In this work, we consider an intermediate case in which the ground waves have wave lengths at least two-three times longer than the structural dimensions, and are long enough to approximate the resulting pseudo-static deformations of the foundation system during the wave passage by an equivalent segment of circular arc. This is illustrated in Figure 19, which shows the plan view of a rectangular foundation deformed into bending by the passing ground wave. Since the significance of such a deformation for structural response can be evaluated with sufficient accuracy, if the radius of curvature of ground deformation is known, in this section, we present a method for evaluating the curvograms (plots of curvature versus time) on ground surface. Trifunac (1990) extended the method for generation of synthetic translational (Trifunac, 1971b; Wong and Trifunac, 1978, 1979), rocking (Lee and Trifunac, 1987), torsional (Lee and Trifunac, 1985) accelerograms, and strain (Lee, 1990) time histories, to obtain curvograms of strong motion.

Let x_1, x_2 and x_3 be the radial, vertical and transverse coordinates. Let c be the apparent phase velocity of wave motion in the radial (x_1) direction. Let u_1, u_2 and u_3 be the displacements in the x_1, x_2 and x_3 directions. Then, the curvature in the vertical plane, $k_2(t)$, is

$$k_2(t) = \frac{\partial^2 u_2 / \partial x_1^2}{\left[1 + (\partial u_2 / \partial x_1)^2\right]^{3/2}} \approx \frac{\partial^2 u_2}{\partial x_1^2} \tag{83}$$

For Rayleigh waves propagating along the ground surface, we have

$$u_2 = U_2(z) e^{ik(x_1 - ct)} \tag{84}$$

so

$$\frac{\partial^2 u_2}{\partial x_1^2} = -k^2 u_2 = -\frac{\omega^2 u_2}{c^2} \tag{85a}$$

and

$$\ddot{u}_2 = \frac{\partial^2 u_2}{\partial t_1^2} = -\omega^2 u_2 \tag{85b}$$

or

$$k_2(t) \approx \frac{\partial^2 u_2}{\partial x_1^2} = \frac{\ddot{u}_2}{c^2} \quad \text{(vertical)} \tag{86a}$$

Likewise, we have

$$k_3(t) \approx \frac{\partial^2 u_3}{\partial x_1^2} = \frac{\ddot{u}_3}{c^2} \quad \text{(transverse)} \tag{86b}$$

$$k_1(t) \equiv 0 \quad \text{(radial)} \tag{86c}$$

as discussed in Trifunac (1990).

1. Estimation of Synthetic Curvograms

From the preceding analysis, it is seen that the curvatures of motion are related to the accelerations, $\ddot{u}_2(t)$ or $\ddot{u}_3(t)$, corresponding to the translational components of motion. As before (by using Equation (2)), we start with the $m-$th mode of surface waves within the frequency band $\omega_n \pm \Delta\omega_n$, associated with the acceleration of vertical motion, $\ddot{u}_2(t)$, whose Fourier transform is given by

$$\mathsf{A}_{nm}(\omega) = \begin{cases} \dfrac{\pi}{2} A_{nm} e^{-i(\omega-\omega_n)t^*_{nm} + i\phi_n} & |\omega - \omega_n| \le \Delta\omega_n \\ 0 & \text{otherwise} \end{cases} \tag{87}$$

and

$$\mathsf{A}_{nm}(-\omega) = \mathsf{A}^*_{nm}(\omega) \tag{88}$$

The inverse transform of Equation (83) is (from Equation (3b))

$$a_{nm}(t) = A_{nm} \frac{\sin \Delta\omega_n (t - t^*_{nm})}{t - t^*_{nm}} \cos(\omega_n t + \phi_n) \tag{89}$$

This represents the contribution of the $m-$th mode of surface waves to acceleration in the frequency band $\omega_n \pm \Delta\omega_n$. The corresponding component of curvature is

$$k_{nm}(t) = \frac{a_{nm}(t)}{C^2_{nm}} = \frac{A_{nm}}{C^2_{nm}} \frac{\sin \Delta\omega_n (t - t^*_{nm})}{t - t^*_{nm}} \cos(\omega_n t + \phi_n) \tag{90}$$

where, as before, $C_{nm} = C_m(\omega_n)$ is the phase velocity of the $m-$th mode of surface waves. The total contributions, $a_n(t)$ and $k_n(t)$, from all modes of surface and body waves in the frequency band $\omega_n \pm \Delta\omega_n$, to acceleration and curvature are, respectively,

$$a_n(t) = \alpha_n \sum_{m=1}^{M} a_{nm}(t) = \alpha_n \sum_{m=1}^{M} A_{nm} \frac{\sin \Delta\omega_n (t - t^*_{nm})}{t - t^*_{nm}} \cos(\omega_n t + \phi_n) \tag{91a}$$

$$k_n(t) = \alpha_n \sum_{m=1}^{M} \frac{a_{nm}(t)}{C^2_{nm}} = \alpha_n \sum_{m=1}^{M} \frac{A_{nm}}{C^2_{nm}} \frac{\sin \Delta\omega_n (t - t^*_{nm})}{t - t^*_{nm}} \cos(\omega_n t + \phi_n) \tag{91b}$$

Recalling that α_n is the scaling factor, as given in Equation (10), the time histories of acceleration and curvature are given by

$$a_i(t) = \sum_{n=1}^{N} a_n(t) = \sum_{n=1}^{N} \alpha_n \left(\sum_{m=1}^{M} A_{nm} \frac{\sin \Delta\omega_n (t - t^*_{nm})}{t - t^*_{nm}} \right) \cos(\omega_n t + \phi_n) \tag{92a}$$

$$k_i(t) = \sum_{n=1}^{N} k_n(t) = \sum_{n=1}^{N} \alpha_n \left(\sum_{m=1}^{M} \frac{A_{nm}}{C^2_{nm}} \frac{\sin \Delta\omega_n (t - t^*_{nm})}{t - t^*_{nm}} \right) \cos(\omega_n t + \phi_n) \tag{92b}$$

with $i = 2$ for the vertical curvature $(k_2(t))$, and $i = 3$ for the transverse curvature $(k_3(t))$. It may be recalled that $k_1(t) \equiv 0$.

By using the corresponding Rayleigh wave phase velocities $C_{nm} = C_m(\omega_n)$ for vertical curvature, and Love wave phase velocities for transverse curvature, their time histories can be computed.

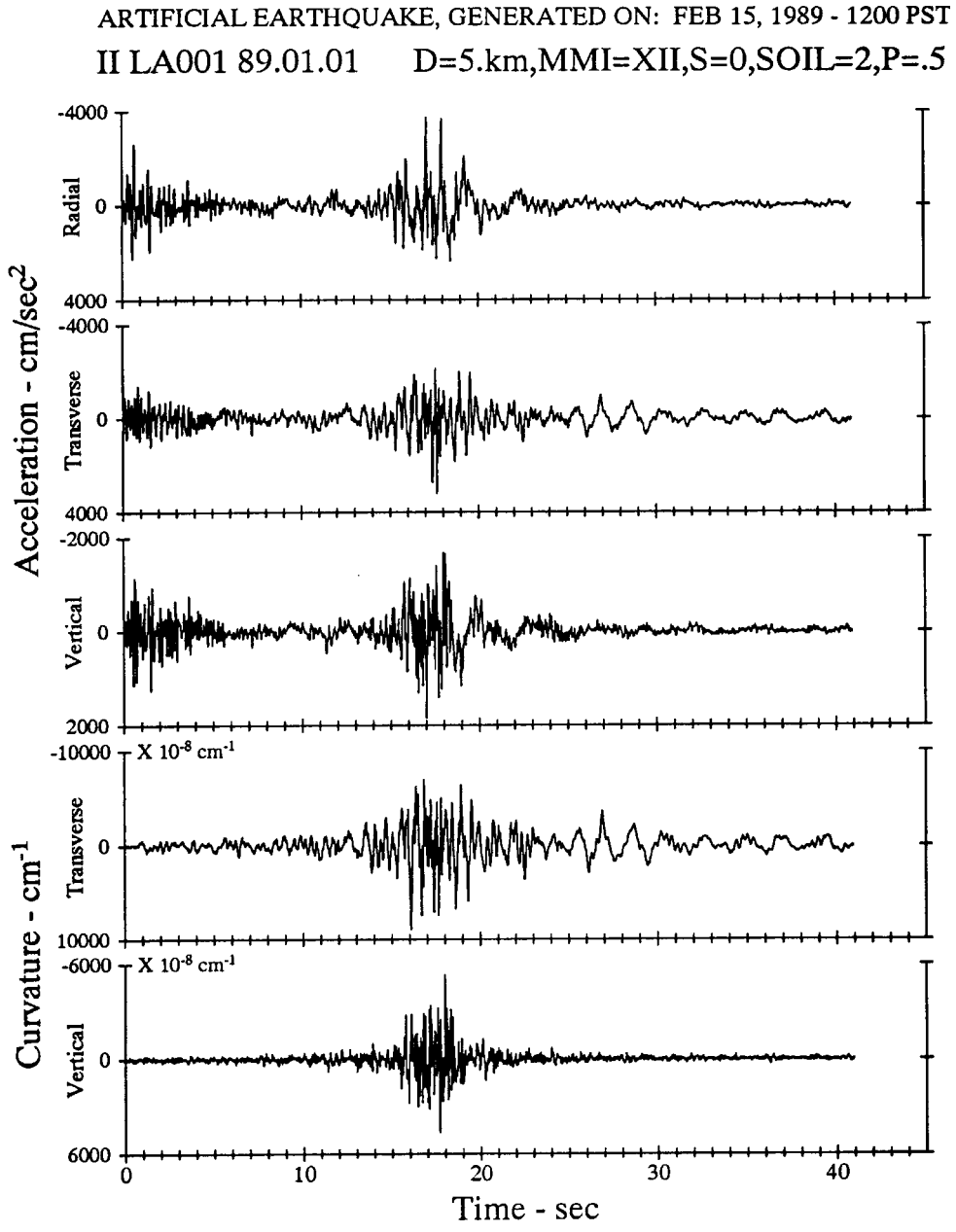

Fig. 20 Artificial earthquake synthetic acceleration and curvature accelerogram: LA001

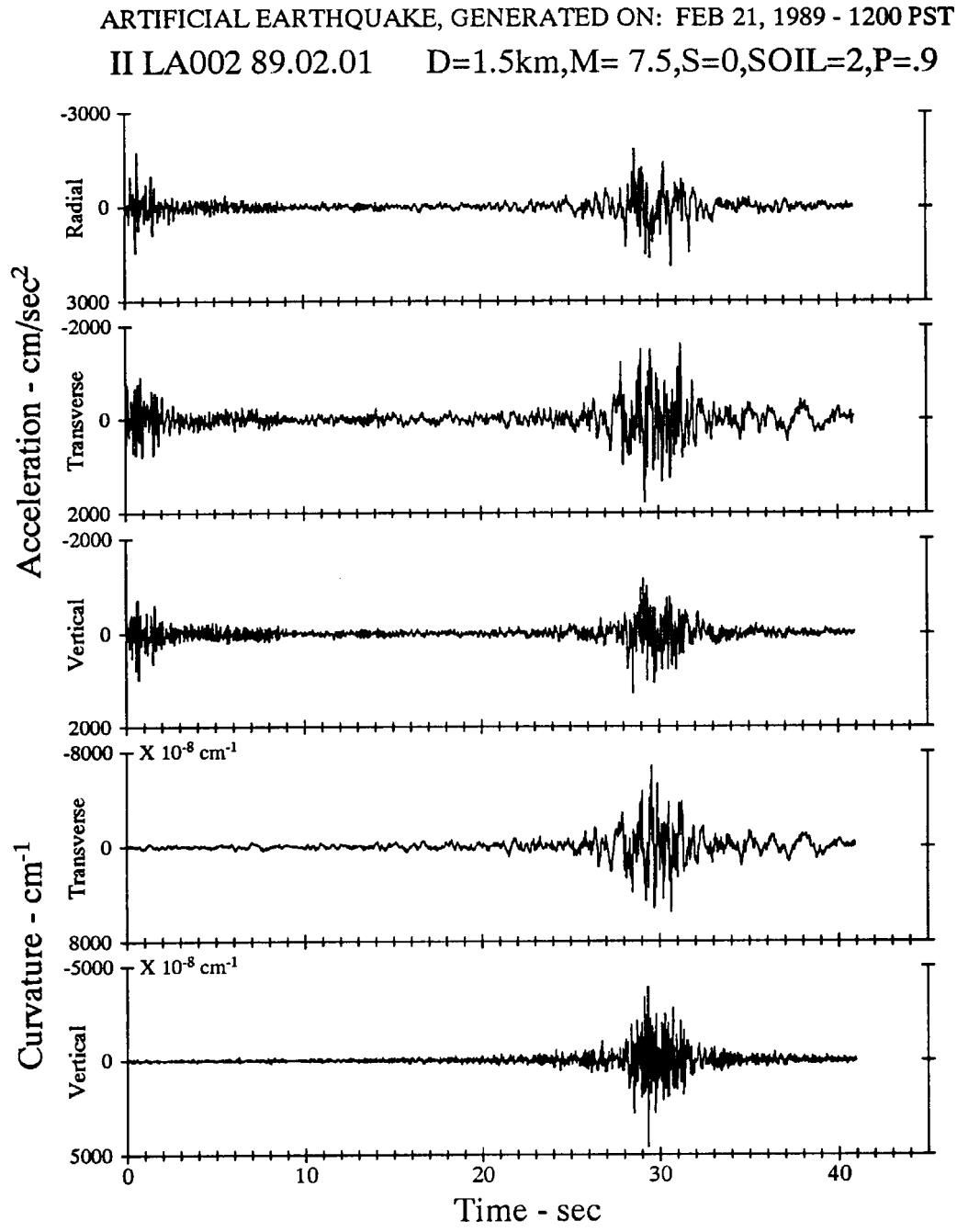

Fig. 21 Artificial earthquake synthetic acceleration and curvature accelerogram: LA002

3. Examples of Synthetic Curvograms

To illustrate the appearance of synthetic curvograms, we consider again the site at Westmoreland in Imperial Valley, California. The local geology and the associated dispersion curves for this site have been used in the preceding sections dealing with the translational, rocking, and torsional accelerograms. For continuity and comparison with the earlier analyses, we consider this site again (Tables 2 and 3). From Equations (86a) and (86b), it is seen that the largest curvature (smallest radius) will be associated with large peak accelerations and with small c, i.e., with "soft" layers near the surface. Thus, in the first example, we consider the site intensity $MMI = XII$ for a source at distance $R = 5$ km. We also assume that the site is on sediments $(s = 0)$ and on deep soil $(s_L = 2)$ (Trifunac, 1989a, 1989b), and compute empirical Fourier spectrum amplitudes, assuming 50% probability of exceedance $(p = 0.5)$. To model $s = 0$ and $s_L = 2$ site conditions, we modify the top layer (in Table 2) to consist of two layers of

thickness 50 m and 130 m, and with shear wave velocities of 50 and 300 m/s, respectively (Table 3). For depths greater than 180 m, we assume the values given in Table 2. Figure 20 shows the resulting radial, transverse, and vertical accelerograms, and the associated transverse and vertical curvograms. The smallest radii of curvature corresponding to $k_{2,\max} = 0.54 \times 10^{-4}\,\mathrm{cm}^{-1}$ and $k_{3,\max} = 0.89 \times 10^{-4}\,\mathrm{cm}^{-1}$ are $\rho_{2,\min} = 185$ m and $\rho_{3,\min} = 112$ m, respectively.

Figure 21 illustrates similar results, but for scaling in terms of magnitude (Trifunac, 1989a). For $M = 7.5,\ R = 1.5$ km, and $p = 0.9,$ the peak curvatures are $k_{2,\max} = 0.46 \times 10^{-4}\,\mathrm{cm}^{-1}$ and $k_{3,\max} = 0.68 \times 10^{-4}\,\mathrm{cm}^{-1},$ and the corresponding radii of curvature are $\rho_{2,\min} = 217$ m and $\rho_{3,\min} = 147$ m.

CONCLUSIONS

A comprehensive method for synthesizing realistic strong motion accelerograms (translations and rotations), strains and curvatures for use in engineering design has been presented. The advantages of this method are that the results are consistent with all known characteristics of the recorded strong shaking. In particular, these accelerograms have non-stationary characteristics in time, which are derived from the known dispersive properties of earthquake waves guided through shallow low-velocity layers of the earth's crust. These dispersive characteristics can be introduced directly as an input into the computer program, and thus can portray directly the geologic environment of each specific site. Other scaling functionals, required for the synthesis of artificial accelerograms presented here, are: (i) the Fourier amplitude spectrum, and (ii) the frequency-dependent duration of strong shaking. These two functionals can be estimated via the empirical scaling relations developed either in terms of earthquake magnitude or in terms of Modified Mercalli Intensity.

It has been shown how the rocking and torsional accelerograms can be generated from the synthetic translational accelerograms, by applying the straightforward exact physical principles of elastic wave propagation. The rotational accelerograms obtained in this way have realistic physical properties, and should resemble actual rotational ground motions, as long as the synthetic translational accelerograms from which those are derived, have such corresponding physical properties.

Using the linear theory of wave propagation, the strain amplitudes can be evaluated exactly in three-dimensions. When local geologic conditions are too complex to model near-surface motions by the equivalent parallel layer models, the method presented here can be modified to give again the exact representation of near-surface translations, rotations, and strains (e.g., see Moeen-Vaziri and Trifunac (1988a, 1988b)).

The above examples illustrate the strain amplitudes implied by the linear theory, and cannot be taken to be "average" or "typical" estimates, for magnitudes, site intensities, or local conditions considered. In general, the strain amplitudes will increase with an overall increase in the strong motion amplitudes, and with a decrease in shear wave velocities of soil and sedimentary layers near the ground surface. Time-dependence of strain components near the ground surface is roughly proportional to the corresponding components of ground velocity, and thus, peak strains will also increase with peak ground velocity.

Finally, the above examples show that the radii of curvature in the range of one to several hundred meters may occur for very large accelerations (1-3 g), near epicenter, and when the local soil and geologic conditions are characterized by very low wave velocities (e.g., 50 m/s). Such conditions correspond only to the instances of exciting very large amplitudes of waves with short wave lengths, and can be expected to occur for soft soil and geologic site conditions near epicenters of earthquakes with high stress drop.

REFERENCES

1. Amin, M. and Ang., A.H.S. (1966). "A Nonstationary Stochastic Model for Strong Motion Earthquakes", Report 306, Struct. Research Series, Dept. of Civil Engng, Univ. of Illinois, Illinois, U.S.A.
2. Baba, K. and Nakashima, H. (1984). "Seismic Response of Uplifting Shear Wall-Flexural Frame Interaction Systems", Proc. 8th World Conf. Earthqu. Engng., Vol. IV, pp. 259-266.

3. Bielak, J. (1978). "Dynamic Response of Nonlinear Building-Foundation System", Earthqu. Engng. Struct. Dynam., Vol. 6, pp. 17-30.
4. Bogdanoff, J.L., Goldberg, J.E. and Bernard, M.C. (1961). "Response of a Simple Structure to a Random Earthquake-Like Disturbance", Bull. Seism. Soc. Amer., Vol. 51, pp. 293-310.
5. Bolotin, V.V. (1960). "Statistical Theory of Aseismic Design of Structures", Proc. 2nd World Conf. Earthqu. Engng, Japan, pp. 1365-1374.
6. Bycroft, G.N. (1960). "White-Noise Representation of Earthquakes", J. Eng. Mech. Div., ASCE, Vol. 86, pp. 1-16.
7. Dravinski, M. and Trifunac, M.D. (1979). "Static, Dynamic and Rotational Components of Strong Shaking near Faults", Report CE 79-06, Dept. of Civil Eng., Univ. of Southern California, Los Angeles, California, U.S.A.
8. Dravinski, M. and Trifunac, M.D. (1980). "Response of Layer to Strike-Slip Vertical Fault", Proc. Engineering Mech. Div., ASCE, No. EM4, pp. 609-621.
9. Goodman, L.E., Rosenblueth, E. and Newmark, N.M. (1955). "Aseismic Design of Firmly Founded Elastic Structures", Trans. ASCE, Vol. 120, pp. 782-802.
10. Goto, H. and Toki, K. (1969). "Structural Response to Nonstationary Random Excitation", Proc. 4th World Conf. Earthqu. Engng, Santiago, Chile.
11. Gupta, I.D. and Trifunac, M.D. (1987). "A Note on Contribution of Torsional Excitation to Earthquake Response of Simple Symmetric Buildings", Earthqu. Engng and Engng Vibrat., Vol. 7, No. 3, pp. 27-46.
12. Gupta, I.D. and Trifunac, M.D. (1988). "A Note on Contribution of Rocking Excitation to Earthquake Response of Simple Buildings", Bull. Indian Soc. Earthquake Tech., Vol. 25, No. 2, pp. 73-83.
13. Gupta, V.K. and Trifunac, M.D. (1990a). "Response of Multistoried Buildings to Ground Translation and Rocking during Earthquakes", J. Prob. Engng Mech., Vol. 5, No. 3, pp. 138-145.
14. Gupta, V.K. and Trifunac, M.D. (1990b). "A Note on Contributions of Ground Torsion to Seismic Response of Symmetric Multistoried Buildings", Earthqu. Engng Engng Vib., Vol. 10, No. 3, pp. 27-40.
15. Gupta, V.K. and Trifunac, M.D. (1990c). "Response of Multistoried Buildings to Ground Translation and Torsion during Earthquakes", Europ. Earthqu. Engng, Vol. IV, No. 1, pp. 34-42.
16. Gupta, V.K. and Trifunac, M.D. (1991). "Effects of Ground Rocking on Dynamic Response of Multistoried Buildings during Earthquakes", Struct. Engng/Earthqu. Engng, JSCE, Vol. 8, No. 2, pp. 43-50.
17. Honda, H. (1957). "The Mechanism of Earthquakes", Geophys. Inst., Tohoku Univ., Vol. 9, No. 5, pp. 1-46.
18. Housner, G.W. (1955). "Properties of Strong Ground Motion Earthquakes", Bull. Seism. Soc. Amer., Vol. 45, pp. 187-218.
19. Hudson, D.E. (1983). "Strong Motion Instrumentation Systems", Proc. Golden Anniversary Workshop Strong Motion Seism., Univ. of Southern California, Los Angeles, California, U.S.A., pp. 73-86.
20. Ishiyama, Y. (1982). "Motions of Rigid Bodies and Criteria for Overturning by Earthquake Excitations", Earthqu. Engng Struct. Dynam., Vol. 10, No. 5, pp. 635-650.
21. Kato, D., Katsumata, H. and Aoyama, H. (1984). "Effect of Wall Base Rotation on Behavior of Reinforced Concrete Frame-Wall Buildings", Proc. 8th World Conf. Earthqu. Engng, Vol. IV, pp. 243-247.
22. Kobori, T. and Shinozaki, I. (1975). "Torsional Vibration of Structure due to Obliquely Incident SH Waves", Proc. 5th European Conf. Earthqu. Engng, Vol. 1, Paper No. 22, pp. 1-5.
23. Kojić, S., Lee, V.W. and Trifunac, M.D. (1988). "Earthquake Response of Arch Dams to Nonuniform Canyon Motion", Report CE 88-03, Dept. of Civil Eng., Univ. of Southern California, Los Angeles, California, U.S.A.
24. Koh, A.S. and Spanos, P.-T.D. (1984). "Seismically Induced Rocking of Rigid Structures", Proc. 8th World Conf. Earthqu. Engng, Vol. IV, pp. 251-258.

25. Lee, V.W. (1979). "Investigation of Three-Dimensional Soil-Structure Interaction", Report CE 79-11, Dept. of Civil Eng., Univ. of Southern California, Los Angeles, California, U.S.A.
26. Lee, V.W. (1990). "Surface Strains Associated with Strong Earthquake Shaking", Proc. JSCE, No. 422/I-14, pp. 187-194.
27. Lee, V.W. and Trifunac, M.D. (1985). "Torsional Accelerograms", Int. J. Soil Dynam. Earthqu. Engng, Vol. 4, No. 3, pp. 132-139.
28. Lee, V.W. and Trifunac, M.D. (1987). "Rocking Strong Earthquake Accelerations", Int. J. Soil Dynam. Earthqu. Engng, Vol. 6, No. 2, pp. 75-89.
29. Lee, V.W. and Trifunac, M.D. (1989). "A Note on Filtering Strong Motion Accelerograms to Produce Response Spectra of Specified Shape and Amplitude", Europ. Earthqu. Engng, Vol. VIII, No. 2, pp. 38-45.
30. Lee, V.W. and Wu, X. (1994a). "Application of the Weighted Residual Method to Diffraction by 2-D Canyons of Arbitrary Shape, I: Incident SH Waves", Soil Dynam. Earthqu. Engng, Vol. 13, No. 5, pp. 355-364.
31. Lee, V.W. and Wu, X. (1994b). "Application of the Weighted Residual Method to Diffraction by 2-D Canyons of Arbitrary Shape, II: Incident P, SV and Rayleigh Waves", Soil Dynam. Earthqu. Engng, Vol. 13, No. 5, pp. 355-364.
32. Luco, J.E. (1976). "Torsional Response of Structures for SH Waves: The Case of Hemispherical Foundation", Bull. Seism. Soc. Amer., Vol. 66, pp. 109-123.
33. Manoogian, M.E. and Lee, V.W. (1996). "Diffraction of SH Waves by Sub-surface Inclusion of Arbitrary Shape", ASCE J. Eng. Mech., Vol. 122, No. 2, pp. 123-129.
34. Moeen-Vaziri, N. and Trifunac, M.D. (1988a). "Scattering and Diffraction of Plane SH-Waves by Two-Dimensional Inhomogeneities", Soil Dynam. Earthqu. Engng, Vol. 7, No. 4, pp. 179-188.
35. Moeen-Vaziri, N. and Trifunac, M.D. (1988b). "Scattering and Diffraction of Plane P and SV Waves by Two-Dimensional Inhomogeneities", Soil Dynam. Earthqu. Engng, Vol. 7, No. 4, pp. 189-200.
36. Nathan, N.D. and MacKenzie, J.R. (1975). "Rotational Components of Earthquake Motions", Can. J. Civil Eng., Vol. 2, pp. 430-436.
37. Newmark, N.M. (1969). "Torsion in Symmetrical Buildings", Proc. 4th World Conf. Earthqu. Engng, Santiago, Chile, A3.19-A3.32.
38. Psycharis, I.N. (1983). "Dynamics of Flexible Systems with Partial Lift-off", Earthqu. Engng Struct. Dynam., Vol. 11, pp. 501-523.
39. Rascon, O.A. and Cornell, A.C. (1969). "A Physically Based Model to Simulate Strong Earthquake Records on Firm Ground", Proc. 4th World Conf. Earthqu. Engng, Santiago, Chile.
40. Richter, C.F. (1958). "Elementary Seismology", Freeman and Co., San Francisco, U.S.A.
41. Rosenblueth, E. (1956). "Some Applications of Probability Theory on Aseismic Design", Proc. World Conf. Earthqu. Engng, Berkeley, California, U.S.A., No. 8, pp. 1-18.
42. Rosenblueth, E. and Bustamante, J.E. (1962). "Distribution of Structural Response to Earthquakes", J. Eng. Mech. Div., ASCE, Vol. 88, pp. 75-106.
43. Shibata, H., Shigeta, T. and Sone, A. (1976). "A Note on Some Results of Observation of Torsional Ground Motions and Their Response Analysis", Bull. Earthqu. Resist. Struct. Res. Center, Vol. 10, pp. 43-47.
44. Todorovska, M.I. and Lee, V.W. (1989). "Seismic Waves in Buildings with Shear Walls or Central Core", ASCE J. Eng. Mech., Vol. 115, No. 12, pp. 2659-2686.
45. Todorovska, M.I. and Trifunac, M.D. (1989). "Antiplane Earthquake Waves in Long Structures", ASCE J. Eng. Mech., Vol. 115, No. 2, pp. 2687-2708.
46. Todorovska, M.I. and Trifunac, M.D. (1990a). "Propagation of Earthquake Waves in Buildings with Soft First Floor", ASCE J. Eng. Mech., Vol. 116, No. 4, pp. 892-900.
47. Todorovska, M.I. and Trifunac, M.D. (1990b). "A Note on Excitation of Long Structures by Ground Waves", ASCE J. Eng. Mech., Vol. 116, No. 4, pp. 952-964.

48. Todorovska, M.I. and Trifunac, M.D. (1992). "Effect of Input Base Rocking on the Relative Response of Long Buildings on Embedded Foundations", Europ. Earthqu. Engng, Vol. VI, No. 1, pp. 36-46.
49. Todorovska, M.I. and Trifunac, M.D. (1993). "The Effects of Wave Passage on the Response of Base-Isolated Buildings on Rigid Embedded Foundations", Report CE 93-10, Dept. of Civil Eng., Univ. of Southern California, Los Angeles, California, U.S.A.
50. Trifunac, M.D. (1971a). "Response Envelope Spectrum and Interpretation of Strong Earthquake Ground Motion", Bull. Seism. Soc. Amer., Vol. 61, pp. 343-356.
51. Trifunac, M.D. (1971b). "A Method for Synthesizing Realistic Strong Ground Motion", Bull. Seism. Soc. Amer., Vol. 61, pp. 1755-1770.
52. Trifunac, M.D. (1972a). "Stress Estimates for San Fernando, California, Earthquake of 9 February 1971: Main Event and Thirteen Aftershocks", Bull. Seism. Soc. Amer., Vol. 62, pp. 721-750.
53. Trifunac, M.D. (1972b). "Tectonic Stress and Source Mechanism of the Imperial Valley, California, Earthquake of 1940", Bull. Seism. Soc. Amer., Vol. 62, pp. 1283-1302.
54. Trifunac, M.D. (1973). "Analysis of Strong Earthquake Ground Motion for Prediction of Response Spectra", Earthqu. Engng Struct. Dynam., Vol. 2, No. 1, pp. 59-69.
55. Trifunac, M.D. (1976). "Preliminary Empirical Model for Scaling Fourier Amplitude Spectra of Strong Ground Acceleration in Terms of Earthquake Magnitude, Source to Station Distance and Recording Site Conditions", Bull. Seism. Soc. Amer., Vol. 66, pp. 1343-1373.
56. Trifunac, M.D. (1979a). "Preliminary Empirical Model for Scaling Fourier Amplitude Spectra of Strong Motion Acceleration in Terms of Modified Mercalli Intensity and Geologic Site Conditions", Earthqu. Engng Struct. Dynam., Vol. 7, pp. 63-74.
57. Trifunac, M.D. (1979b). "A Note on Surface Strains Associated with Incident Body Waves", Bull. EAEE, Vol. 5, pp. 5-95.
58. Trifunac, M.D. (1982). "A Note on Rotational Components of Earthquake Motions for Incident Body Waves", Soil Dynam. Earthqu. Engng, Vol. 1, No. 1, pp. 11-19.
59. Trifunac, M.D. (1989a). "Dependence of Fourier Spectrum Amplitudes of Recorded Strong Earthquake Accelerations on Magnitude, Local Soil Conditions and on Depth of Sediments", Earthqu. Engng Struct. Dynam., Vol. 18, No. 7, pp. 999-1016.
60. Trifunac, M.D. (1989b). "Empirical Scaling of Fourier Spectrum Amplitudes of Recorded Strong Earthquake Accelerations in Terms of Magnitude and Local Soil and Geologic Conditions", Earthqu. Engng Engng Vib., Vol. 9, No. 2, pp. 23-44.
61. Trifunac, M.D. (1990). "Curvograms of Strong Ground Motion", ASCE J. Eng. Mech., Vol. 116, No. 6, pp. 1426-1432.
62. Trifunac, M.D. (1993). "Long Period Fourier Amplitude Spectra of Strong Motion Acceleration", Soil Dynam. Earthqu. Engng, Vol. 12, No. 6, pp. 363-382.
63. Trifunac, M.D. (1994). "Q and High Frequency Strong Motion Spectra", Soil Dynam. Earthqu. Engng, Vol. 13, No. 3, pp. 149-161.
64. Trifunac, M.D. (1995a). "Pseudo Relative Velocity Spectra of Earthquake Ground Motion at Long Periods", Soil Dynam. Earthqu. Engng, Vol. 14, No. 5, pp. 331-346.
65. Trifunac, M.D. (1995b). "Pseudo Relative Velocity Spectra of Earthquake Ground Motion at High Frequencies", Earthqu. Engng Struct. Dynam., Vol. 24, No. 8, pp. 1113-1130.
66. Trifunac, M.D. (1997). "Differential Earthquake Motion of Building Foundations", J. Structural Eng., ASCE, Vol. 123, No. 4, pp. 414-422.
67. Trifunac, M.D. and Brady, A.G. (1975). "A Study on the Duration of Strong Earthquake Ground Motion", Bull. Seism. Soc. Amer., Vol. 65, pp. 581-626.
68. Trifunac, M.D. and Anderson, J.G. (1977). "Preliminary Empirical Models for Scaling Absolute Acceleration Spectra", Report CE 76-03, Dept. of Civil Eng., Univ. of Southern California, Los Angeles, California, U.S.A.

69. Trifunac, M.D. and Lee, V.W. (1978). "Dependence of the Fourier Amplitude Spectra of Strong Motion Acceleration on the Depth of Sedimentary Deposits", Report CE 78-14, Dept. of Civil Eng., Univ. of Southern California, Los Angeles, California, U.S.A.
70. Trifunac, M.D. and Lee, V.W. (1985). "Preliminary Empirical Model for Scaling Fourier Amplitude Spectra of Strong Ground Acceleration in Terms of Earthquake Magnitude, Source to Station Distance, Site Intensity and Recording Site Conditions", Report CE 85-03, Dept. of Civil Eng., Univ. of Southern California, Los Angeles, California, U.S.A.
71. Trifunac, M.D. and Novikova, E.I. (1994). "State of the Art Review on Strong Motion Duration", 10th Europ. Conf. Earthqu. Engng, Vienna, Austria. Vol. 1, pp. 131-140.
72. Trifunac, M.D. and Novikova, E.I. (1995). "Duration of Earthquake Fault Motion in California", Earthqu. Engng Struct. Dynam., Vol. 24, No. 6, pp. 781-799.
73. Trifunac, M.D. and Todorovska, M.I. (1997a). "Response Spectra and Differential Motion of Columns", Earthquake Eng. Structural Dyn., Vol. 26, No. 2, pp. 251-268.
74. Trifunac, M.D. and Todorovska, M.I. (1997b). "Northridge, California, Earthquake of 17 January 1994: Density of Pipe Breaks and Surface Strains", Soil Dynamics Earthquake Eng., Vol. 16, No. 3, pp. 193-207.
75. Trifunac, M.D. and Todorovska, M.I. (2001). "A Note on Useable Dynamic Range in Accelerographs Recording Translation", Soil Dynamics Earthquake Eng., Vol. 21, No. 4, pp. 275-286.
76. Trifunac, M.D., Todorovska, M.I. and Ivanovic, S.S. (1996). "Peak Velocities, and Peak Surface Strains during Northridge, California, Earthquake of 17 January 1994", Soil Dynamics Earthquake Eng., Vol. 15, No. 5, pp. 301-310.
77. Trifunac, M.D. and Westermo, B.D. (1976a). "Dependence of Duration of Strong Earthquake Ground Motion on Magnitude, Epicentral Distance, Geologic Conditions at the Recording Station and Frequency of Motion", Report CE 76-02, Dept. of Civil Eng., Univ. of Southern California, Los Angeles, California, U.S.A.
78. Trifunac, M.D. and Westermo, B.D. (1976b). "Correlations of Frequency Dependent Duration of Strong Earthquake Ground Motion with the Modified Mercalli Intensity and the Geologic Conditions at the Recording Stations", Report CE 77-03, Dept. of Civil Eng., Univ. of Southern California, Los Angeles, California, U.S.A.
79. Tso, W.K. and Hsu, T.I. (1978). "Torsional Spectrum for Earthquake Motions", Earthqu. Engng Struct. Dynam., Vol. 6, pp. 375-382.
80. Wong, H.L. and Trifunac, M.D. (1978). "Synthesizing Realistic Strong Motion Accelerograms", Report CE 78-07, Dept. of Civil Eng., Univ. of Southern California, Los Angeles, California, U.S.A.
81. Wong, H.L. and Trifunac, M.D. (1979). "Generation of Artificial Strong Motion Accelerograms", Earthquake Engineering Structural Dynamics, Vol. 7, pp. 509-527.
82. Yim, C.S., Chopra, A.K. and Penzien, J. (1980). "Rocking Response of Rigid Blocks to Earthquakes", Earthqu. Engng Struct. Dynam., Vol. 8, No. 6, pp. 565-587.